Universitat de les Illes Balears

BACHELOR'S THESIS

GRAVITATIONAL WAVE SIGNALS FROM COALESCING BINARY BLACK HOLE AND NEUTRON STAR SYSTEMS

Miquel Duran Pou

Degree in Physics

Faculty of Sciences

Academic Year 2020-21

GRAVITATIONAL WAVE SIGNALS FROM COALESCING BINARY BLACK HOLE AND NEUTRON STAR SYSTEMS

Miquel Duran Pou

Bachelor's Thesis

Faculty of Sciences

University of the Balearic Islands

Academic Year 2020-21

Key words:

General relativity, gravitational waves, black holes, neutron stars, waveform modelling, match filtering, equation of state, tidal effects.

Thesis Supervisor's Name: Sascha Husa

Tutor's Name (if applicable): Sascha Husa

The University is hereby authorized to include this project in its institutional repository for its open consultation and online dissemination, for academic and research purposes only.	Author		Supervisor	
	Yes	No	Yes	No
	☒	☐	☒	☐

Abstract

The aim of this project is to present the current state of Neutron Star-Black Hole system detections and give a sense of how they can be studied and what can be learned from them. For that, it walks the reader through the basics of General Relativity and Gravitational Waves theory, with an overview of linearized theory, the wave solutions of the Einstein Equations and the quadrupole approximation. Then, the physics of the formation and composition of the sources that radiate gravitational waves are explained in order to show how they affect the emitted radiation. Namely, these sources are black holes, neutron stars and white dwarfs in binary systems, and detecting and understanding their effects on the gravitational wave radiation would help to better comprehend them and allow the inference of their equation of state. In addition, it describes the process of detection and subsequent data analysis and reviews the models utilized to characterize gravitational waveforms using analytical and numerical solutions. This leads to the discussion of the gravitational-wave signals detected so far, specifically the only two Neutron Star-Black Hole detections to date. Finally, a comparison of the agreement between different waveform models is used to better understand their reliability and the significance of possible systematic errors in terms of the current and future sensitivity of gravitational wave detectors.

Contents

1 Introduction

Gravitational wave astronomy has brought about a breakthrough in the study of the universe, unveiling information hitherto concealed. Gravitational Waves (GWs) allow new ways for testing General Relativity and the detection of processes invisible by any other means, and they can also be used to complement data from other "messengers", such as photons, neutrinos and cosmic rays, providing in this way even more information about their sources.

The first direct gravitational wave detection was made on September 14, 2015 by the Advanced Laser Interferometer Gravitational-Waves Observatory (LIGO). The signal was discovered to be generated by a black hole binary of initial masses of $36^{+5}_{-4}M_{\odot}$ and $29^{+4}_{-4}M_{\odot}$. Since then, three observation "runs" (O1, O2, O3) have already been conducted with the advanced generation of interferometric GW detectors. Breaks between observation runs were exploited to upgrade the detectors and increase their sensitivity. The third observation run was split into two: O3a, which ended on October 1st 2019, and O3b, which was suspended on March 26 2020, almost a month prior to the scheduled end, on account of the COVID-19 pandemic. The next observation run, O4, is scheduled to start after April 2022 and the detectors are intended to achieve the planned design sensitivity, for after which further detector upgrades have already been mapped out.

While the first two runs had a total of 10 binary black hole (BBH) and a single binary neutron star (BNS) detections, O3a has confidently detected 37 BBH mergers and 2 possible neutron star-black hole (NSBH) mergers. Also, already 17 detections from O3b have been publicly announced, of which two have been identified as NSBH mergers, GW200105 and GW200115 (Abbott et al., 2021). In this thesis we will discuss these recent results regarding the discovery of NSBH systems, and compare different models of the signals, in order to test for systematic errors in the signal models.

1.1 Gravitational Waves Theory

Gravitational waves are distortions of spacetime that travel in the form of transverse waves at the speed of light. They are caused by aspherical accelerating mass, and carry information about the dynamics of the sources and gravity itself. However, it turns out that spacetime is very rigid, consequently the magnitude of these spacetime distortions is very small, and gravitational wave detectors can only measure waves that originated from violent, highly energetic cosmic events. Not only is it very difficult for matter to distort spacetime, but likewise gravitational waves also transfer very little energy to matter. Their observation is thus not based on transfer of energy, but on the distance modulation of freely falling (at least in one dimension) test masses. As a consequence of the very small interaction with matter, gravitational waves propagate undisturbed over long distances and cannot be "shielded", e.g. by dust clouds, in the same way electromagnetic (EM) waves are. Binary systems are one of the most effective mechanisms to accelerate masses. As it is, all signals directly observed have been so far generated by the coalescence of compact binaries. Moreover, the more heavy and compact the source, the easier the gravitational radiation it emits will be detected, and therefore black hole binaries have had the most presence in detections to date.

As mentioned before, the first gravitational wave detection was not possible until 2015, although their existence had already been predicted by Albert Einstein in 1916 and experimental evidence was found in the 1980s by observing orbital energy loss in the binary pulsar PSR B1913+16, which was discovered in 1974 by Hulse and Taylor (Hulse and Taylor, 1975).

Einstein's theory of General Relativity originates in the need to make gravitation consistent with special relativity while also being consistent with Newton's Laws in an appropriate limit. This is achieved by formulating gravity as a geometric property of a dynamic, curved space-time. The intrinsic curvature is described by the Riemann tensor, R^c_{acb}, which has the property that parallel transport of a vector along a closed path rotates the vector by an amount proportional to the Riemann tensor. The Riemann tensor vanishes if and only if the space is flat. Simpler quantities can be computed from the Riemann tensor, such as the Ricci tensor and scalar.

According to General Relativity, test particles move along geodesics, which is the generalization of a straight line in curved space. That curvature is caused by the momentum and energy of radiation and matter, and the relation between these attributes is manifested in the Einstein Field Equations (EFE),

$$R_{ab} - \frac{1}{2}Rg_{ab} = \frac{8\pi G}{c^4}T_{ab}. \tag{1.1}$$

Here, R_{ab} is the Ricci curvature tensor, R is the scalar curvature, g_{ab} is the metric tensor, G is Newton's gravitational constant, c the speed of light in vacuum and, finally, T_{ab} is the stress-energy tensor. Note that both the left and right hand sides of Eq. (1.1) are divergence free, which expresses local energy conservation. The Ricci curvature (or Ricci tensor), which is a combination of derivatives of the Christoffel coefficients, can be derived as a contraction of the Riemann tensor:

$$R_{ab} = R^c_{acb} = \frac{\partial \Gamma^c_{ab}}{\partial x^c} - \frac{\partial \Gamma^c_{ab}}{\partial x^b} + \Gamma^c_{ab}\Gamma^d_{cd} - \Gamma^c_{ad}\Gamma^d_{bc}, \tag{1.2}$$

where the quantities Γ^c_{ab} are the Christoffel symbols,

$$\Gamma^c_{ab} = \frac{g^{ad}}{2}\left(\frac{\partial g_{db}}{\partial x^c} + \frac{\partial g_{dc}}{\partial x^b} - \frac{\partial g_{bc}}{\partial x^d}\right). \tag{1.3}$$

Finally, the scalar curvature R is the trace of the Ricci curvature tensor, $R = g^{ab}R_{ab} = R^a_a$, and can be interpreted as the rotation of a vector under parallel transport over a closed path on a surface. If the spacetime is flat, the vector does not rotate and R=0. In vacuum, the stress-energy tensor T_{ab} is zero, which results in the vacuum Einstein equations: $R_{ab} = 0$.

The EFE are very complex partial differential equations, but can be extremely simplified when written in tensor algebra. It is these equations which describe and predict phenomena such as black holes (BH), gravitational waves (GW) or the expansion of the universe.

2 Gravitational wave observation of binary systems

2.1 Linearized Theory

The simplest starting point for a discussion of GWs is linearized gravity. Spacetimes that only slightly deviate from a flat space can be described as the flat metric, η_{ab}, with a

perturbation, expressed by the metric perturbation, h_{ab}, which will obey the following condition.

$$g_{ab}(x) = \eta_{ab} + h_{ab}(x), \qquad ||h_{ab}|| \ll 1. \tag{2.1}$$

Here η_{ab} is defined to be diag(-1,1,1,1), and the condition for h_{ab} means the perturbation is assumed weak and the coordinate system approximately inertial and Cartesian. Consequently, terms of higher order than linear in h_{ab} will be discarded.

We will first discuss the propagation of gravitational waves through the universe, e.g. in the vicinity of a detector, which is far from the source and where the amplitude of the waves can therefore be considered very small. We thus postpone the consideration of sources and, for simplicity, consider the propagation of the waves in a vacuum. We insert Eq. (2.1) into $R_{ab}=0$, and expand to first order in h_{ab}. The first term is the Ricci tensor of flat space, which vanishes, and the second is its first-order perturbation, for which we need to compute the Christoffel symbols:

$$\delta\Gamma^c_{ab} = \frac{1}{2}\eta^{cd}\left(\partial_b h_{da} + \partial_a h_{db} - \partial_d h_{ab}\right), \quad \delta R^c_{ab} = \partial_c \delta\Gamma^c_{ab} + \partial_b \delta\Gamma^c_{ac} + O(h^2) \tag{2.2}$$

Since the zeroth component of the Christoffel symbols vanishes due to the components of η_{ab} being constant, only the first-order perturbation terms remain. Combining the two equations from (2.2), we obtain the linearized vacuum EFE:

$$\delta R_{ab} = \frac{1}{2}\left(-\Box h_{ab} + \partial_a V_b + \partial_b V_a\right) = 0. \tag{2.3}$$

Here, $\Box = \eta^{ab}\partial_a\partial_b$ stands for the d'Alembertian, which is the flat-space wave operator, and the vector V_a is defined as $V_a = \partial_c h^c_a + \frac{1}{2}\partial_a h^c_c$. The equation (2.3) corresponds to a set of ten linear, partial differential equations for $h_{ab}(x)$. Notice that indices on perturbations can be raised and lowered with the flat space metric.

A gauge symmetry exists, which corresponds to the freedom of choosing coordinates, and can be identified with changes of coordinates in the form of $x^a \longrightarrow x'^a = x^a + \xi^a(x)$, where ξ^a are four arbitrary functions that must obey $|\partial_a\xi_a| \sim |h_{ab}|$ to respect the condition on $|h_{ab}|$ (Eq. (2.1)). Applying the transformation to the metric yields

$$g'_{ab}(x') = \frac{\partial x^c}{\partial x'^a}\frac{\partial x^d}{\partial x'^b}g_{cd}(x) = \eta_{ab} + h'_{ab} = \eta_{ab} + (h_{ab} - \partial_a\xi_b - \partial_b\xi_a). \tag{2.4}$$

This gauge transformation is analogous to the Lorenz gauge in electromagnetism, where the gauge freedom in the vector potential, $A_a \longrightarrow A_b + \partial_a\Lambda$, is used to impose that the vector potential is divergence free. Therefore, similarly to that case we now choose the four arbitrary functions $\xi^a(x)$ so $V'_a = 0$, thus cancelling both terms with derivatives of the vector V in Eq. (2.3). Additionally, this condition is consistent with energy-momentum conservation in linearized theory, $\delta^a T_{ab} = 0$.

Defining $\xi^a(x)$ reduces the 10 degrees of freedom left in the symmetric 4x4 tensor h_{ab} to 6. In GR, this gauge is called *harmonic gauge*, and greatly simplifies the linearized vacuum EFE:

$$\Box h_{ab} = 0 \tag{2.5}$$

which, since $\Box = -(1/c^2)\delta_0^2 + \nabla^2$, admit a superposition of plane waves as a solution, *gravitational waves*, that propagate at the speed of light:

$$h_{ab} = a_{ab}(\mathbf{k})e^{ikx}, \tag{2.6}$$

3

where $k^\mu = (\omega/c, \mathbf{k})$ and $\omega/c = |\mathbf{k}|$. The tensor a_{ab}, or *polarization tensor*, has the same properties as h_{ab} (4x4 symmetric) and gives the amplitude of the wave components, which are not arbitrary but can be simplified by making further gauge choices in addition to harmonic gauge. Explicit calculations show that the metric perturbations are purely spatial ($h^{0i} = 0$) and traceless ($h^a_a = 0$). Moreover, the conditions of the Lorentz gauge imply that the spatial metric perturbation are transverse and that h^{00} is time independent. Therefore, it can be interpreted as the static gravitational interaction, or Newtonian potential of the source, which in our case would be zero. This gauge is called the *transverse traceless gauge (TT gauge)* and, adding these 4 conditions to the harmonic gauge, reduces the degrees of freedom of our problem to 2. Thus, choosing the z axis parallel to the direction of propagation, both degrees of freedom are completely defined by the amplitudes of the perturbation in the x-y plane, and are usually called "plus" and "cross" polarizations.

$$h^{TT}_{ab}(x) = \begin{bmatrix} 0 & 0 & 0 & 0 \\ 0 & h_+ & h_\times & 0 \\ 0 & h_\times & -h_+ & 0 \\ 0 & 0 & 0 & 0 \end{bmatrix} e^{ikx}. \tag{2.7}$$

In order to understand how gravitational waves are generated, at least in a weak field situation, we have to consider the linearized Einstein equations in the presence of matter fields, i.e. when the energy momentum tensor is not zero. One can again use the Lorenz gauge and obtain

$$\Box h_{ab} = -\frac{16\pi G}{c^4} T_{ab}. \tag{2.8}$$

Using the property that stress-energy tensor T_{ab} is divergence free, in weak fields the influence of the stress-energy tensor on the gravitational field can be approximated by its time-time component T^{00}, which can be interpreted as the energy density of matter ρ,

$$\rho = T^{00}. \tag{2.9}$$

For consistency with weak gravitational fields we also restrict ourselves to low-velocity sources, meaning the velocities inside the source are considered to be much smaller than the speed of light c. It is then possible to write the gravitational wave signal in terms of time derivatives of the quadrupole moment Q^{ij} of the mass density of the source,

$$Q^{ij} = \int d^3x \rho(t, \mathbf{x})(x^i x^j - \frac{1}{3} r^2 \delta^{ij}), \tag{2.10}$$

obtaining

$$\left[h^{TT}_{ij}(t, \mathbf{x})\right]_{quad} = \frac{1}{r} \frac{2G}{c^4} \ddot{Q}^{TT}_{ij}(t - r/c). \tag{2.11}$$

Here i, j are spatial indices and $t - r/c$ is the retarded time.

The fact that the mass quadrupole generates the leading order multipole of the gravitational radiation field can be understood as follows: when performing the multipole expansion, we see that the first term, mass monopole, relates to the total mass-energy in the system, which must be conserved. Similarly, the second term, mass dipole, relates to the center of mass of the system and its derivative to the system's momentum, which must also be conserved. Thus the lowest remaining order affecting gravitational radiation generation is the mass quadrupole.

Furthermore, the quadrupole approximation can be used to find a simple expression for the radiated energy, or luminosity, of a source:

$$\left[\frac{dE}{dt}\right]_{quad} = \frac{G}{5c^5}\langle \dddot{Q}_{ij}^{TT}\ \dddot{Q}_{ij}^{TT}\rangle. \tag{2.12}$$

The average is understood as a temporal average over several periods of the GW.

2.2   Sources

2.2.1   The basic physics of binary systems in general relativity

A first approximation to gravitational wave emission by binary systems is to consider circular Keplerian orbits and the quadrupole approximation for the emitted gravitational wave signal, from which one can compute the radiated power. The loss of energy will cause the orbital radius to decrease, but we will consider the transition of orbit to be slow and adiabatic. In the Newtonian approximation and center-of-mass frame, the dynamics of two point-like compact stars, with masses m_1, m_2 and positions $\mathbf{r}_1$ and $\mathbf{r}_2$, reduces to a one-body problem with mass equal to the reduced mass $\mu = m_1 m_2/(m_1 + m_2)$, and equation of motion $\ddot{\mathbf{r}} = -(Gm/r^3)\mathbf{r}$, where $m = m_1 + m_2$ is the total mass and $\mathbf{r} = \mathbf{r}_2 - \mathbf{r}_1$, the relative coordinate.

In this context, one can extract from Eq. (2.11) expressions for the amplitudes of the plus and cross polarization terms of the stress metric:

$$h_+(t) = \frac{4G\mu\omega_s^2 R^2}{rc^2}\frac{1+cos^2\theta}{2}cos(2\omega_s t), \quad h_\times(t) = \frac{4G\mu\omega_s^2}{rc^2}cos\theta sin(2\omega_s t), \tag{2.13}$$

where ω_s is the orbital frequency and R, the orbital radius. Notice that the gravitational wave frequency is twice the frequency of the source, $\omega_{GW} = 2\omega_s$. Furthermore, computing the quadrupole moment of the binary system and inserting it into equation (2.12), one can write the quadrupole radiation power emitted during the inspiral as

$$P = \left[\frac{dE}{dt}\right]_{quad} = \frac{32c^5}{5G}\left(\frac{GM_c\omega_{GW}}{2c^3}\right)^{10/3}. \tag{2.14}$$

The loss of energy caused by GW emission forces the orbital radius to decrease over time ($E_{orbit} \propto -R^{-1}$) and, according to Kepler's third law, if R decreases, ω_s increases. On the other hand, if ω_s increases, the power radiated increases (2.14) making R to decrease further. This runaway process leads, after a sufficiently long time-scale, to the coalescence of the binary system.

Subsequent development yields expressions for the time evolution of the GW frequency:

$$f_{GW}(\tau) = \frac{1}{\pi}\left(\frac{5}{256\tau}\right)^{3/8}\left(\frac{GM_c}{c^3}\right)^{-5/8}, \quad \tau = \frac{5}{256}(\pi f_{GW})^{-8/3}\left(\frac{GM_c}{c^3}\right)^{-5/8}, \tag{2.15}$$

where $M_c = \mu^{3/5}m^{2/5}$ is the *chirp mass*, t_{coal} is the coalescence time from a time of reference and τ is the time until coalescence ($\tau = t_{coal} - t$). Notice that it is possible to express the dependence on the intrinsic source parameters through the single parameter M_c.

We see from the above equations that both the amplitude and frequency of the waveform increase as the coalescence is approached (see Figure 1 right panel for a graphical

representation). This behaviour is referred to as "chirping", since when translated into air pressure waves, the sound it produces resembles the chirp of a bird.

We can now discuss real scenarios by inserting the numerical values in equations (2.15):

$$f_{GW}(\tau) = 135 Hz \left(\frac{1.21 M_\odot}{M_c} \right)^{5/8} \left(\frac{1s}{\tau} \right)^{3/8}, \quad \tau = 2.18s \left(\frac{1.21 M_\odot}{M_c} \right)^{5/3} \left(\frac{100 Hz}{f_{GW}} \right)^{8/3},$$
(2.16)

where $1.21 M_\odot$ has been taken as a reference for M_c, which corresponds to a binary system with two $1.4 M_\odot$ stars. Considering this reference case, at 10 Hz we detect the radiation emitted at about $\tau = 17$ min to coalescence; at 100 Hz, from the last two seconds, and at 1 kHz, we get the radiation from the last few milliseconds. When $f_{GW} = 1$ kHz, the separation between the two $1.4 M_\odot$ bodies is $R \simeq 33$km (Eq. 2.19), which can only be reached by very compact bodies, such as black holes or neutron stars. For the only two currently published NSBH detections, the chirp mass is around $M_c = 3 M_\odot$, which produces a signal that enters the detectors' sensitive frequency bandwidth (10 Hz) about 4 min before the merger.

Another interesting quantity is the number of cycles the interferometers are able to detect in terms of their sensitivity, because the more cycles before merger are detected, the more information to characterize the waveform we get. Thus, for a binary with slowly varying orbital frequency, i.e. in the inspiral, the number of cycles $\mathcal{N}_{cyc}$ is described as

$$\mathcal{N}_{cyc} = \frac{1}{32\pi^{8/3}} \left(\frac{GM_c}{c^3} \right)^{-5/3} \left(f_{min}^{-5/3} - f_{max}^{-5/3} \right) \simeq 1.6 \times 10^4 \left(\frac{10\,Hz}{f_{min}} \right)^{5/3} \left(\frac{1.2 M_\odot}{M_c} \right)^{5/3},$$
(2.17)

where $\left(f_{min}^{-5/3} - f_{max}^{-5/3} \right) \simeq f_{min}^{-5/3}$ is assumed, as is typically the case. Setting f_{min} to 10 Hz, we get thousands of cycles for low mass binaries such as the NSBH detections. However, for higher total mass binaries such as a BBH with $m_1 = 1000 M_\odot$, $m_2 = 100 M_\odot$, we can only detect the last dozen cycles.

Now, using equation (2.15) and Kepler's third law, we can find an ordinary differential equation that relates the increase of frequency and the shrinking of the orbital radius,

$$\frac{\dot{R}}{R} = -\frac{2}{3} \frac{\dot{\omega}_{GW}}{\omega_{GW}} = -\frac{1}{4\tau},$$
(2.18)

which integrates to the evolution of the orbital separation over time,

$$R(\tau) = R_0 \left(\frac{\tau}{\tau_0} \right)^{1/4},$$
(2.19)

where R_0 is the value of R at the initial time t_0, and $\tau_0 = t_{coal} - t$.

In the inspiral phase, the flat background approximation used in all of the above computation is valid, and therefore our model of slow adiabatic succession of quasi-circular orbits driven by the emission of gravitational radiation is still accurate. However, in the Schwarzschild geometry exists a minimum of the radial distance beyond which the gravitational field is rather strong, affecting the dynamics of the binary system when the two objects get close. Mainly, this effect is observed as a plunge of the two stars toward each other, caused by the fact that the Schwarzschild geometry no longer allows for circular orbits. In the left panel of Figure 1 we can see the evolution of the orbital radius taking only the quadrupole power loss into account (Eq. 2.19). Considering strong
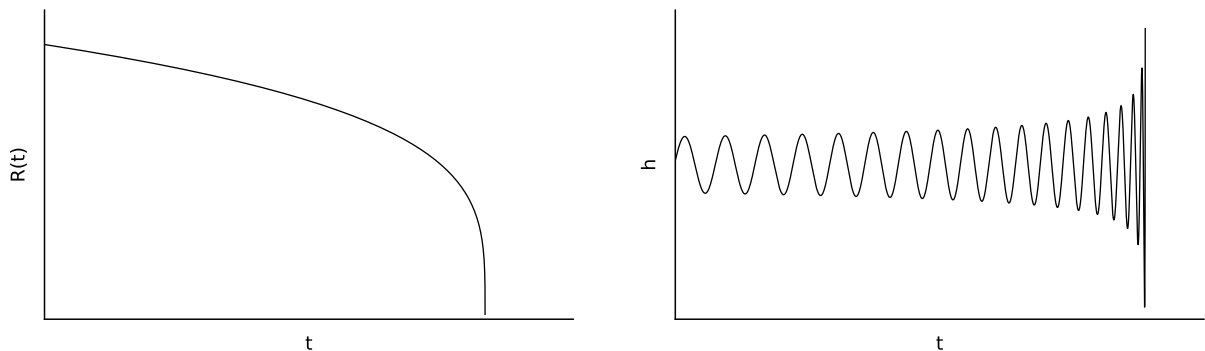
Figure 1: Left panel: The time evolution of the separation $R(t)$ between the two bodies until coalescence. Right panel: The evolution over time of the GW amplitude in the inspiral phase of a binary. Both computed in the lowest-order Newtonian approximation.

gravitational fields, we would see a more sudden transition from the inspiral phase to the plunge and merger. The limit at which that would happen, i.e. the orbital radius inside which the orbits can no longer be supposed circular, is called Innermost Stable Circular Orbit (ISCO) and can be defined by the value of the Schwarzschild radial coordinate $r = r_{ISCO}$, located at

$$r_{ISCO} = \frac{6Gm}{c^2} \tag{2.20}$$

Therefore, the waveform computed above is only valid up to a maximum frequency f_{max}. Thus, from the third Kepler's law one can compute the source frequency f_s that marks the end of the inspiral phase,

$$(f_s)_{ISCO} = \frac{1}{6\sqrt{6}(2\pi)}\frac{c^3}{Gm}\,. \tag{2.21}$$

Inserting the numerical values,

$$(f_s)_{ISCO} = 2.2 \text{ kHz} \left(\frac{M_\odot}{m}\right), \tag{2.22}$$

we can study the maximum frequency for some standard systems. This is of interest because in order to be detected, the frequency must lie within the detectors sensitive band, which will be discussed in Section 2.3. For instance, a NS binary with total mass $m \simeq 2.8M_\odot$ (corresponding to two typical $1.4M_\odot$ neutron stars) yields $(f_s)_{ISCO} \sim 800$ Hz, while a BH-BH system with a total mass $m = 10M_\odot$ yields $(f_s)_{ISCO} \sim 200$ Hz. For reference, f_s is of the order of mHz when two supermassive BHs with $m \sim 10^6 M_\odot$ coalesce.

Writing out the power radiated (2.14) per unit solid angle and integrating over the time domain, we can use the Fourier transform of h_+ and $h_\times$ to obtain $dE/df d\Omega$ which, after integrating over a sphere surrounding the source, yields the energy spectrum

$$\frac{dE}{df} = \frac{\pi^{2/3}}{3G}(GM_c)^{5/3}f^{-1/3}. \tag{2.23}$$

Integrating up to the maximum GW frequency f_{max}, which we can approximately set at $f_{max} = 2(f_s)_{ISCO}$ for the quadrupole limit of the inspiral phase, and inserting numerical

values, we see that the total energy radiated during the inspiral phase depends only on the reduced mass μ and is

$$\Delta E_{rad} \sim 8 \times 10^{-2} \mu c \,. \tag{2.24}$$

For the two detected NSBH binaries, GW200115 and GW200105, the reduced masses are around $1.2 M_\odot$ and $1.6 M_\odot$, and the total energy radiated during the inspiral phase is $\Delta E_{rad} = 5.73 \cdot 10^{37} J$ and $\Delta E_{rad} = 7.64 \cdot 10^{37} J$, respectively, which are huge amounts of energy.

Up until now, we have seen simple solutions of binary coalescence with the lowest-order Newtonian approximation. However, more accurate and complex solutions can be found by going further along the Newtonian expansion and applying higher-order multipole moment terms to the description of the fields generated by still slowly moving and weakly self-gravitating sources. This post-Newtonian (PN) expansion is widely used by actual waveform models (section 2.4).

On top of that, it is useful, as in any other radiation problem, to study the angular dependence of the radiation. This can be accomplished by combining both strain amplitude tensors into a complex quantity, $h(t, \mathbf{r}) = h_+(t, \mathbf{r}) + ih_\times(t, \mathbf{r})$. Then, taking into account that, at large distances to the source, the strain is inversely proportional to that distance

$$h(t, \mathbf{r}) = \frac{h_0(t, \hat{\mathbf{r}})}{r} + O(r^{-2}) \,, \tag{2.25}$$

the complex tensorial quantity $h(t, \mathbf{r})$ can be expanded in terms of spin-weighted spherical harmonics (SWSHs) with spin weight $s = -2$ (Goldberg et al., 1967),

$$h(t, \mathbf{r}) = \frac{1}{r} \sum_{l,m} h^{l,m}(t) Y_{l,m}^{-2}(\theta, \phi) \,. \tag{2.26}$$

Here, the coordinates θ and ϕ stand for the standard polar angles on the unit sphere, thus giving the direction $\hat{\mathbf{r}}$. Given this expression, it is sensible to study directly the mode amplitudes $h_{l,m}(t)$ instead of the strain function in any direction, since handling a few functions that depend solely on time is significantly simpler than dealing with a single function depending on two angles and time.

In the non-relativistic quadrupole aproximation (see Eq. 2.13) one can demonstrate that binary systems without orbital precession emit gravitational waves mainly in the direction orthogonal to the orbital plane, i.e. $\theta = 0, \pi$. We can follow this symmetry aligning the z-axis with that direction, which shows that mode amplitudes obey an inherent hierarchy, its value decreasing with l and with $|m|$ in each l. The dominant modes of the wave are then those described by the $(l = 2, m = |2|)$ spherical harmonics.

2.2.2 Compact objects in general relativity

When stars run out of fuel for nuclear fusion, they contract until new equilibrium between pressure and gravitation are found, or, if no such equilibrium exists, they undergo complete collapse to a black hole. In any case, the new object is much more compact than the original star, and stellar remnants such as white dwarfs, neutron stars, or black holes, or in fact any object with a similar level of compactness, i.e. a similar ratio of mass to radius, is called a compact object. Stars typically have angular momentum and are thus not exactly spherically symmetric, however it turns out that the basic principles of the formation of compact objects can indeed already be understood in spherical symmetry.

The metric for the vacuum region of a spherically symmetric spacetime, e.g. the region outside of a compact object, had already been found in 1916 by Karl Schwarzschild (Schwarzschild, 1916), and is called the Schwarzschild solution. The line element is

$$ds^2 = -\left(1 - \frac{2GM}{rc^2}\right)dt^2 + \frac{dr^2}{1 - \frac{2GM}{rc^2}} + r^2 d\Omega^2, \tag{2.27}$$

where M is the total mass and $d\Omega^2 = d\theta^2 + sin^2\theta d\varphi^2$.

Spherical symmetry and stationarity restrain our freedom to choose a set of coordinates. By assuming $d\Omega^2$ to be a part of the invariant interval ds^2, ϕ and θ are constrained to be interpreted as variables labeling directions in space. Furthermore, ϕ and θ have a natural geometric interpretation as angles, and the time coordinate t directly expresses a symmetry (the metric does not depend on it). Reparameterizing t in any non-trivial way would make the metric depend on t and hide the symmetry. However, no natural choice exists for the radial coordinate r, which needs to be chosen carefully. The Schwarzschild metric can be restricted to the coordinate spheres $t = t_0$, $r = r_0$, given by $g|_{t=t_0, r=r_0} = r_0^2 d\Omega^2$, which is positive and definite. This means with the choice for r made above, the coordinate spheres are actual geometric spheres with area $A = 4\pi r_0^2$. Consequently, the radial coordinate chosen in Eq. (2.27) possesses a geometric interpretation in terms of the surface area of nested round spheres, and can be described by it: $r = \sqrt{\frac{A}{4\pi}}$. It can also be defined in terms of the measured circumference around the black hole at fixed r, θ and t: $\mathcal{C} = \int ds = r \int d\phi = 2\pi$. Both ways, the r coordinate has a useful physical interpretation, and becomes radial distance in the flat-space limit.

The Schwarzschild line element shows two singular points, at $r = 0$, and $r = 2GM/c^2$. The singularity at $r = 0$ is a true physical singularity, where the curvature diverges, while the singularity at $r = 2GM/c^2$ is only a coordinate singularity. Inspecting the line element one can see that when the radius r approaches the value of $r = 2GM/c^2$, i.e. at the "Schwarzschild radius", the metric component g_{tt}, and thus the norm of the timelike basis vector $(\partial/\partial t)^a$, vanishes. The interpretation is that this timelike vector becomes null, so you would need to move outwards at the speed of light to stay in place. Therefore, anything past the Schwarzschild radius will not be able to escape the gravitational pull, not even light. This boundary is what is now known as event horizon: the surface which causal influences can cross only inwards. The region of space-time delimited by that surface, from which neither matter nor radiation can escape, is what we call a black hole.

Until now, we have discussed the static, spherically symmetric solution, Schwarzschild geometry, but it can be generalized by including charge and angular momentum. The spacetime geometry for an axisymmetric, charged black hole is called the Kerr-Newman solution (Newman and Janis, 1965), but it can be simplified by considering angular momentum or charge to be zero, yielding the Reissner–Nordström (Reissner (1916) and Nordström (1918)) and Kerr (Kerr, 1963) solutions respectively. Astrophysical black holes are expected to have non-zero spin, since stars are generally rotating. And since any existent net charge is expected either to attract the opposite and neutralize or be expelled by the intense electromagnetic fields around rotating astrophysical bodies, we will focus on the rotating, uncharged axially-symmetric solution, also called Kerr metric or Kerr geometry. By the no-hair theorem (see Israel (1967) and Israel (1968)), hair being a metaphor for extra parameters other than mass, charge and angular momentum, Kerr black holes can be parametrized by just mass and spin.

We now consider a spherically symmetric region of spacetime that contains matter. We start off with a general time-invariant, spherically symmetric metric as ansatz, quite

similar to the Schwarzschild metric/line element:

$$ds^2 = -e^{-2\phi(r)}dt^2 + \frac{dr^2}{1 - \frac{2m(r)}{r}} + r^2 d\Omega^2, \tag{2.28}$$

where the functions $m(r)$ and $\phi(r)$ are chosen for convenience to simplify the interpretation of the g_{tt} and g_{rr} metric components.

Inserting the ansatz (2.28) into the Einstein equations yields ordinary differential equations for the functions $m(r)$ and $\phi(r)$. The equation for $m(r)$ can directly be integrated to

$$m(r) = \int_0^r 4\pi r'^2 \rho(r') dr', \tag{2.29}$$

which gives the total mass enclosed in a sphere of radius r. Notice that given a mass distribution where $2m(r) = r$ is satisfied at a certain r, the radial component of the line element diverges (2.28) and, therefore, the star collapses. The equation for $\phi(r)$ reads

$$\frac{d\phi(r)}{dr} = \frac{m(r) + 4\pi r^3 P/c^2}{r\left[r - \frac{2m(r)G}{c^4}\right]}. \tag{2.30}$$

In the Newtonian limit $c \to \infty$ this becomes the equation for the Newtonian gravitational potential,

$$\phi'_N = \frac{m(r)}{r^2},$$

which justifies our ansatz for $\phi(r)$.

We have thus obtained equations for the metric components in terms of the functions $m(r)$ and $\phi(r)$ and yet unspecified mass density $\rho(r)$ and pressure $P(r)$. We assume for simplicity that our matter takes the form of an ideal fluid, which has the energy momentum tensor

$$T_{ab} = \rho u_a u_b + P(g_{ab} + u_a u_b). \tag{2.31}$$

This specific choice of energy momentum tensor obeys the general property of an energy momentum tensor, which is the law of differential conservation of energy and linear momentum,

$$\nabla_a T^{ab} = 0. \tag{2.32}$$

In addition we will assume that both the matter density and pressure are non-negative,

$$\rho, \quad P \geq 0. \tag{2.33}$$

Finally, by plugging the tensor field for a perfect fluid (2.31) into the EFE and using Eq. (2.32), one can derive the Tolman–Oppenheimer–Volkoff (TOV) equation for the structure of a static, spherically symmetric relativistic star (Wald, 1984):

$$\frac{dP}{dr} = -(\rho + P)\frac{m(r) + 4\pi r^3 \rho}{r\left[r - 2m(r)\right]}. \tag{2.34}$$

The variables P and ρ are related by an equation of state (EoS) specific to the star, which is necessary to solve the TOV equation. Taking the non-relativistic limit, the TOV equation becomes the Newtonian hydrostatic equation:

$$\frac{dP}{dr} = -\rho\frac{m(r)}{r^2}. \tag{2.35}$$

10

Comparing Eq. (2.34) to Eq. (2.35), we see both the pressure term and the $4\pi r^3 \rho$ term are positive quantities that contribute to internal pressure needing to be higher to hold against gravitational collapse. Furthermore, one can solve the equation for the general potential $\phi(r)$ by finding solutions for equations (2.29) and (2.34) and plugging them into (2.30), which is decoupled from the other two.

Due to the complexity of characterizing a realistic EoS (which will be briefly discussed below) and solving the TOV equation with it, we may consider a uniform density star to find an exact solution:

$$\rho(r) = \begin{cases} \rho_0 & (r \leq R) \\ 0 & (r > R) \end{cases}, \tag{2.36}$$

where R is the radius of the star. By definition of surface of a bound star in vacuum, we can define the boundary condition on the pressure $P(r = R) = 0$. This is not a very accurate estimate, but very dense objects such as the center of a neutron star can be roughly approximated to constant.

The expression for $P(r)$ in Newtonian physics for a constant density spherical object is quite simple: $P(r) = \frac{2\pi}{3}\rho_0(R^2 - r^2)$, but no so much in general relativity. Therefore, we will restrict ourselves to study only the central pressure, $P_c = P(r = 0)$. The TOV equation yields

$$P_c = \rho \frac{\sqrt{1 - \frac{2M}{R}} - 1}{1 - 3\sqrt{1 - \frac{2M}{R}}}. \tag{2.37}$$

Notably, P_c diverges when $\frac{M}{R} = \frac{4}{9}$. This is called the Buchdahl limit, and yields an upper limit $R < 2.25M$, just a little bit larger than the Schwarzschild radius. Similar results for more complicated scenarios indicate the Buchdahl limit to be universal. Moreover, from this expression follows a relation to compute the maximal mass of a body, which was the original purpose of the TOV equation,

$$M_{max} \propto \frac{1}{\sqrt{\rho_0}}, \tag{2.38}$$

meaning the higher the central density, the smaller the maximal mass.

Different compact objects can be found throughout the universe, each with different composition and therefore varying densities. Using the results extracted above, one can approximate a maximal mass for each type of them.

These compact objects are usually cores of stars that have died out. Stars are held up by the energy generated by fusion reactions: hydrogen atoms combine into helium, those into lithium an so on until iron, after which fusion becomes endothermic. As a result, the star starts running out of elements to fuse, the energy generated decreases and the internal pressure can no longer hold against gravitational collapse. If the stellar mass is typically under $9M_\odot$, the core collapses into a white dwarf. Otherwise, the collapse triggers an explosive reaction called supernova, which expels several solar masses of material. Sometimes, the core will coalesce into something even more compact than white dwarfs, namely neutron stars or black holes.

White dwarfs, as stellar cores that no longer undergo fusion reaction, have no source of energy except stored thermal energy, which causes the faint luminosity they give off. Instead, the process preventing their collapse is the pressure generated by Pauli's exclusion principle, which states that no two fermions can occupy the same quantum state.

Thus, the electrons in a white dwarf behave as a Fermi gas, holding it against the self-gravitational pull. Electron-degenerate matter density is of the order of $10^9 \, kg/m^3$, making white dwarfs 4 orders of magnitude denser than the core of the Sun.

The results of the TOV equation and physics of degeneracy yield a maximal mass for white dwarfs over which the electron degeneracy pressure can no longer prevent the collapse (Chandrasekhar limit). This critical mass is about $1.44M_\odot$, also called the Chandrasekhar mass due to its relation to the Chandrasekhar limit (Chandrasekhar, 1931). If this mass is surpassed, the core collapses further and reaches temperatures higher than $10^9 K$, giving protons and electrons enough energy to form neutrons via electron capture, thus releasing a flood of neutrinos. Neutrons, being also fermions, also obey the Pauli exclusion principle, though the fact that they are more massive than electrons (and therefore have a much shorter wavelength at a given energy) allows for a smaller separation between the degenerate neutrons. Consequently, a degenerate neutron gas can reach pressures much higher than that of a degenerate electron gas. When core densities reach nuclear density of $4 \times 10^{17} \, kg/m^3$, a combination of neutron degeneracy pressure and strong force repulsion stops the contraction, the neutrinos produced in the neutrons' creation flings the infalling outer layer of the star outwards, expelling several solar masses of material. This explosion is known as a supernova, and its luminosity is akin to that of entire galaxies and can take various weeks until it completely fades away. Supernovae can emit gamma ray bursts (GRB), which are the most energetic electromagnetic events known in the universe, lasting from several milliseconds to hours. After the initial flare of gamma rays, light of longer wavelength is commonly emitted for a longer period of time ("afterglow"), which permits the observation of the aftermath of supernovae explosions.

However, core collapse isn't the only way to cause a supernova. In a binary system, the core of a white dwarf can reach the ignition temperature for carbon fusion as it approaches the critical mass by accreting mass from its companion, or by merger if the companion is another white dwarf. Within a few seconds of the start of nuclear fusion, a significant part of the white dwarf undergoes a runaway fusion reaction, which releases sufficient energy to cause a supernova explosion (Wikipedia, 2021). This type of supernova, supernova Ia, is particularly interesting because it produces a fairly consistent peak luminosity due to the fixed critical mass at which a white dwarf will explode. Therefore, type Ia supernovae can be used as standard "candles" to measure the distance to their host galaxies, or to study the expansion of the universe and dark energy.

After the explosion, the core can coalesce back and settle into a neutron star or, if the remaining mass exceeds the maximal mass for neutron stars ($2M_\odot \sim 3M_\odot$, depending on how high the rotational breakup limit is assumed), the internal pressure gives in to gravitational collapse and a black hole is formed. This formation channel, per the conservation of angular momentum of the original "progenitor" star, usually produces rapidly rotating compact stars, since the radius of the spinning cloud of material is extremely reduced in the coalescence. Highly magnetized spinning neutron stars (and sometimes white dwarfs), or *pulsars*, emit pulses of electromagnetic radiation in the radio spectrum. This radiation is shot out of their magnetic poles so, due to misalignment between the spin axis and magnetic axis, detection is only possible when that direction points towards the observer, giving the pulsed appearance and evoking the behaviour of a lighthouse. When pulsars are found in binary systems, the orbital shift usually causes the beam to no longer pass over us, thus becoming invisible to our telescopes. This is what happened to the Hulse and Taylor pulsar (Hulse and Taylor, 1975), which can no longer be seen from the Earth. Since neutron stars are very dense and have short, regular rotational periods, the pulses

are produced at very precise intervals, which range from milliseconds to seconds. Pulsars, like supernovae, are also candidates for the source of ultra-high-energy cosmic rays.

Before the discovery of gravitational waves, phenomena like supernovae, GMB and pulsar radiation were the only window to study observed or theoretical objects like black holes, neutron stars, and white dwarfs. Whereas now, gravitational wave detection has broadened multimessenger astronomy, allowing us to observe the same event through different lenses and learn much more about their nature, the matter they are made of and their possible equations of state. An example of this is the discovery of event GW170817 (Abbott et al., 2017). It consisted in the detection through GWs of the inspiral and merger of a binary system of two neutron stars (BNS), combined with the observation of an EM counterpart, 170817A, detected by Fermi-GBM 1.7s after the merger. This observation confirms the hypothesis of a neutron star merger and links these with short gamma ray burst through direct evidence for the first time. Short GRB appear to originate when the development of a resonance between their crust and core, product of the immense tidal forces experienced in the seconds that precede the merger, causes the outer layer of the star to bust (Tsang et al., 2012). Transient counterparts across the electromagnetic spectrum where later spotted in the same direction and distance, further supporting the interpretation of this event as the merger of a BNS system. This unprecedented joint electromagnetic and gravitational observation proves an example of the future of multimessenger astronomy, and casts some light on gravitation, dense matter, cosmology and astrophysics.

Compact Binary Coalescence (CBC) are key sources for gravitational-wave astronomy, since, as explained in Subsection 2.2.1, the emission of GWs reduces the distance between the two compact bodies, augmenting the orbital frequency and therefore increasing the total energy carried away by gravitational radiation. Thus, orbital motion is a particularly effective way to accelerate astrophysical objects. Furthermore, compact objects allow for very small separations, and so, at the final stages of the coalescence, they can emit GWs of high frequencies and energies, which are easier to detect. However, the ability to observe binary systems is dependent on their mass, since, as we will see in Section 2.3, ground-based detectors have a specific frequency band of sensitivity and frequency is indirectly proportional to the total mass. Black Hole Binaries (BHB) are the most effective known source of gravitational waves, seeing that they are the most compact astrophysical objects, and can therefore orbit at the smallest separations and highest frequencies. Compact binaries can have one of two origins: "dynamical interaction" or "isolated binary evolution". The first happens when two objects pass close enough to each other to fall into a stable orbital motion, and are more likely to occur in dense stellar environments such as globular clusters; the latter means the two objects were already in orbit before going supernova and becoming compact objects. To distinguish between them, spin and orbital angular momentum alignment give a strong hint. If a NSBH system, for example, was formed by isolated binary evolution, we would expect the neutron-star to orbit around the black hole equatorial plan. In contrast, formation by dynamical capture should not have a preferred direction of the spin, and therefore the NS orbit could have any orientation relative to the black hole's equatorial plane. For supermassive BH binaries, arbitrary orientation is expected, since they have to be formed by the merging of lighter ones at the core of galaxies, which collide at random angles.

Per the aforementioned no-hair theorem, the parameter space of a BHB can be defined by eight parameters, namely two masses and two spins. For eccentric orbits, two more parameters would be needed to characterize the orbit (its orientation and eccentricity).

Such orbits are sparse, however, because they are prone to rapidly circularize when no other interactions are present (Peters, 1964). Therefore, efforts of current data analysis are focused on circular binaries, which need no further parameters due to the relation between the separation between the two masses and the velocity. In vacuum general relativity, geometrized units ($G = c = 1$) are commonly used, since the lack of other fundamental constants allows the mass to act as purely a scale parameter. The parameter space is therefore further reduced to seven, since the information of both masses can be encoded within the mass ratio, $q = m1/m2 \geq 1$.

The coalescence of two compact objects can be dissected into three phases. The first is the inspiral, where they revolve around each other for long periods of time, slowly loosing orbital energy by the runaway GW emission process explained in Subsection 2.2.1. This ends with the plunge and subsequent merger, where both objects combine into an unstable one. This final compact object oscillates, emitting GWs until it stabilizes into, if it has enough mass, a Kerr black hole. This last stage is called the ringdown, since it consists in an exponential decrease of GW amplitude: from its maximum in the merger to the effective null amplitude of a stable Kerr black hole. Good qualitative descriptions of the inspiral and ringdown signals can be provided by analytic approximation techniques, but no so much during the plunge and merger. The simplest version of these calculations is the one viewed in the previous subsection (2.2.1) based on Newtonian orbital dynamics and Einstein's quadrupole formula.

However, for a more accurate description of GWs emitted by binaries with at least one material body (i.e. not a black hole), other phenomena need to be taken into account. We will center our attention on neutron star-black hole (NSBH) binaries, as they are the focus of this project. The key difference between black holes and material bodies during the inspiral is that the latter deform significantly under tidal stress. That is, the gravitational pull on the neutron star is greater at the closest point than at the furthest, and this difference gives rise to a strain on the neutron star material. This tidal interaction modifies the inspiral rate and can in principle be observed in the gravitational wave signal. The rotation of the star causes this strain to be applied in different directions, falling into a pattern of expansions and contractions in synchrony with the neutron star's rotational period (the same process that caused the loss of rotational energy of our moon and consequent synchronization with its orbital period). In the latest stages of the coalescence, when distances between the bodies are short and the gravitational pull strongest, the tidal deformations can become too violent for the star to hold against, breaking into a cloud of neutron star material that is absorbed by the other object. This process, called tidal disruption, would be seen as a sudden decrease in the GW amplitude at high frequency and observing it could provide valuable information about the extreme form of matter that makes up neutron stars.

2.3 Data Analysis

In essence, gravitational wave detectors are Michelson-Morley interferometers. They measure the gravitational wave strain as a difference of length of their arms, which leads to an interference between the originally in-phase laser beams that travel through each arm. This transmits an optical signal proportional to the strain of the wave (see Figure 2 for a simplified bluprint). However, these length variations are 10^{-21} times smaller than the 4km-arms, and thus comparable to a thousandth of the width of a proton, so the phase shift of the two beams is of the order of a trillionth of their wavelength, making the inter-
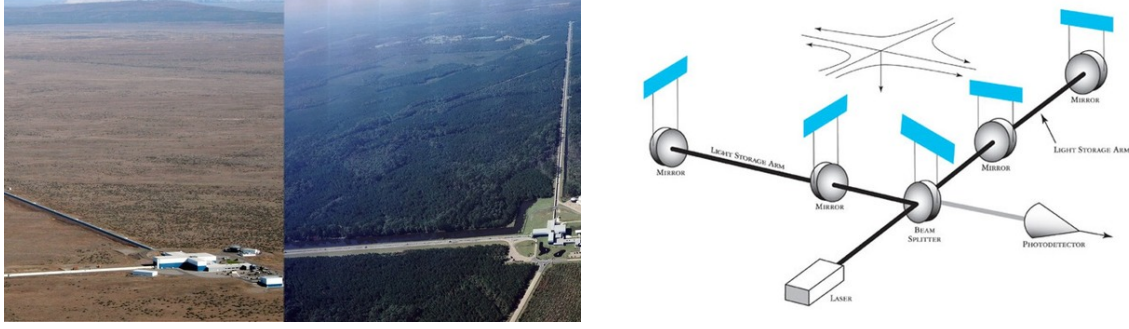
Figure 2: Left panel: Aereal views of the the LIGO Hanford and LIGO Livingston interferometers. Right panel: Basic schematic of LIGO's interferometers. Images recovered from LIGO Caltech.

ference signal variations extremely faint. As a consequence, great effort is needed to reach the required sensitivity and reduce the effects of thermal and seismic noise, other noise sources and optical phase fluctuations. Some of the measures taken are using very smooth mirrors held by silica threads to gain precision in the detection of the phase variation, extremely low-pressure vacuum chambers to reduce interactions with the megawatt laser beams, and building different detectors at different sites: LIGO Livingston and Hanford (See Figure 2, left panel), Virgo and Kagra, which not only helps eliminate local noises, but also allows for a more precise location of the source;.

Despite the efforts to reduce detection noise, it still embodies most of the detector's output. So the only way to extract a signal much smaller than the floor of the noise is to know, at least to same level of accuracy, the form of $h(t)$, aside from the typical scales of variations of the noise, and use bayesian statistics and match-filtering techniques to recover the gravitational wave signal. Thus, we describe the detector's output as $d(t) = s(t) + n(t)$, where $s(t)$ is what we expect to be a GW signal, and $n(t)$ is the detector noise. The *spectral noise density* or *power spectral density* (PSD) $S_n(f)$ is defined so that the ensemble average over different noise realizations of $n^2(t)$, $\langle n^2(t)\rangle$, is obtained integrating this function over the physical range of frequencies $0 \leq f < \infty$, rather than from $-\infty$ to ∞,

$$\langle n^2(t)\rangle = \langle n^2(t=0)\rangle = \int_{-\infty}^{\infty} df\,df' \langle n^*(t)n(f')\rangle = \int_0^{\infty} df\, S_n(f)\,. \tag{2.39}$$

If $n(t)$ is dimensionless, $S_n(t)$ must be in Hz^{-1} and therefore the noise generated inside the detector can be characterized by the *spectral strain sensitivity*, which has units of $Hz^{-1/2}$ and can be computed with $\sqrt{S_n(f)}$, called the *spectral strain amplitude*. See Figure 3, which shows the sensitivity upgrade from the initial detectors (green) to the Advanced interferometers used in O1. Even still, the sensitivity of these earth-based detectors is limited at low and high frequencies, and the most sensitive frequency band is between 100 Hz and 300 Hz. To gain access to lower frequency gravitational radiation and a more flat spectral sensitivity curve overall, a space-based interferometer will be needed, which is planned to be launched in 2034. The Laser Interferometer Space Antena (LISA) will consist of three satellites in an heliocentric orbit working as an effective triangular Michelson-Morley interferometer, and will be able to detect not only binaries of compact objects within the Milky Way, but also extreme mass ratio inspirals, mergers of massive black holes at the centre of galaxies, and possibly other cosmological sources, such as the initial stages of the Big Bang, and speculative astrophysical objects like domain boudaries
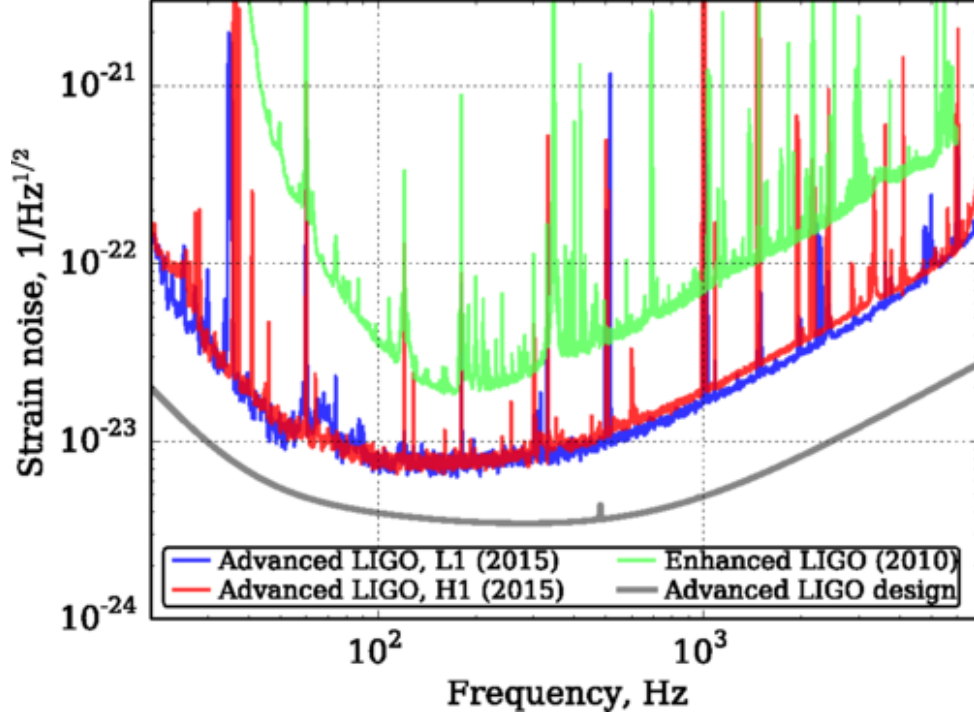
Figure 3: The spectral sensitivity of the total strain noise in units of strain per $\sqrt{Hz}$. Image recovered from Martynov et al. (2016).

and cosmic strings (Amaro-Seoane et al., 2013). Furthermore, it is expected that LISA will be able to anticipate the LIGO detections by a few weeks or months (see Eq. (2.17)), resolving about 100 binaries before they are detected on Earth at merger, the time of which it will be able to accurately predict beforehand and locate the direction of the event with very high precision. This will greatly improve the possibilities of finding EM counterpart events (Amaro-Seoane et al., 2017).

As mentioned above, a data analysis strategy often used is to perform match filtering (see e.g. Maggiore (2008), ch. 7 for textbook development). The main idea of this method consists in applying many different templates $h(t, \theta_N)$, where $\theta_N = \theta_1, \theta_2, \ldots, \theta_n$ is the discrete parameter space characterizing the shape of the pulse and its temporal width, to the data by computing the scalar product between the template and the output of the detector $d(t)$, chosen so the signal-to-noise ratio (SNR) is maximized. Constructing the scalar product between two real variables as

$$(A|B) = 4 \cdot Re \int_0^\infty df \frac{\tilde{A}^*(f)\tilde{B}(f)}{S_n(f)} , \qquad (2.40)$$

the SNR can then be defined as the coefficient of S, the expected value of a quantity which depends on the template and the output of the detector, and N, its RMS value when the signal is absent. Thus, applying the SNR definition to the scalar product yields

$$\frac{S}{N} = \frac{(h|d)}{\sqrt{(h|h)}}, \qquad (2.41)$$

from which follows that the optimal value of SNR is $\sqrt{(h|h)}$, and so

$$\left(\frac{S}{N}\right)^2_{opt} = 4 \int_0^\infty df \frac{|\tilde{h}(f)|^2}{S_n(f)}. \qquad (2.42)$$

16

For Gaussian noise, optimizing the SNR over the time shift and complex phase parameters of the templates $h(t, \theta_N)$ would suffice to recover the signal from under the noise floor. In reality, however, most events surpassing the set minimal SNR would be due to non-Gaussian transients and "glitches", so significant effort goes into reducing the number of glitches, though they cannot be completely removed. Consequently, the analysis must also exert methods to discern signal from noise transients, such as χ^2 consistency tests with coherent and coincidence searches (see Harry and Fairhurst (2011)).

Notice that the SNR is dependant on the amplitude of $d(t)$, which is useful for many types of analyses, but if we are only interested in the overlap of the shapes of $h(t, \theta_N)$ and $d(t)$, we must then also divide by the amplitude of $d(t)$:

$$m = \frac{(h|d)}{\sqrt{(h|h)(d|d)}} \, . \tag{2.43}$$

After optimizing over time shift and complex phase (rotation), which does not affect the shape of the waveform, m becomes the match between $h(t, \theta_N)$ and $d(t)$, which goes from 0 to 1.

Data analysis for compact binary signals observed by current ground based detectors is commonly carried out as a two-step process: first, searches are performed (see e.g. Usman et al. (2016)) to detect as many events as possible while minimizing the false alarm rate. The most sensitive search techniques are based on matched filtering with banks of astrophysically plausible signals. Such banks typically contain around 10^5 templates $h(t, \theta_N)$, where the templates are chosen sufficiently dense in the parameter space to not loose more than 10% of the signals. It is also possible to perform generic transient searches, where no specific template bank is assumed, and events are identified based on their amplitude above the background and the evolution of the frequency in time. This allows to discover unmodelled signals. Both matched filter and unmodelled searches assign a statistical significance to candidate signals, which is typically quantified as a false alarm rate (FAR). When a matched filter search is performed, the templates that yield the highest SNR provide a rough estimate of the source parameters.

For detected events a more detailed procedure is then used to compute the best estimate of the source parameters, as well as error estimates. This step is usually called "parameter estimation" and uses the framework of Bayesian statistics and Bayesian inference (see e.g. Veitch et al. (2015)). For this step using a fixed template bank would be prohibitively expensive, and algorithms like Markov-Chain-Monte-Carlo or nested sampling are used to perform random walks that sample the parameter space and allow to compute expectation values, variances, and related quantities. Typically 10^7– 10^9 evaluations of waveform models are required to accurately determine the source parameters and determine the specifics of the GW sources. Said parameters are the intrinsic parameters (masses and spins) and the extrinsic parameters (polarization, inclination, distance, sky location and coalescence phase). Bayesian statistics are applied to infer a probability distribution of the source parameters (of the two coalescing bodies and of the final object), as well as the total energy radiated, giving the most likely values and the error estimates.

2.4 Waveform models

In a first approximation, i.e. neglecting tidal effects and when disruption does not occur, BH models can be used to describe any compact-object binary. Even so, to precisely model their gravitational waveforms a combination of analytical and numerical methods is

needed: while the inspiral and ring-down stages of the BH coalescence can be described by perturbative techniques, the merger requires a non-perturbative treatment and thus numerical solutions of Einstein's equations. Such numerical simulations are computationally very expensive and so it is computationally prohibitive to densely sample the parameter space of BH coalescences. In the last 15 years the waveform modelling community has constructed a "zoo" of waveform models, combining analytical and numerical- relativity results to describe all stages of the coalescence. This has dramatically improved the sensitivity of searches for GWs from BH binaries and the accuracy of estimating the source parameters. Two main families of these models exist: the time domain family based on the effective one-body approach, "EOBNR" (Rettegno et al., 2020), which mostly use integration of PN energy flux to indirectly calculate the waveforms; and the phenomenological frequency domain family, IMRPhenom (Inspiral-Merger-Ring-down) (Ajith et al., 2011), which make use of physical insight to directly model the waveforms, and therefore being much faster than the former. Each of these have been upgraded over the years (e.g. SEOBNRv4 (Rettegno et al., 2020) or PhenomP and PhenomX (Pratten et al., 2020)), and the differences between them have diffused; although for computations in the presence of noise (such as searches or match-filterings, for instance), it is most sensible to make use of frequency domain-based models since, aside from being faster, noise is more easily characterized in the frequency domain. Moreover, hybrid models (MacDonald et al., 2011) are able to use perturbative theory in the inspiral phase and numerical relativity (NR) for the plunge merger and ring-down, granting more precision while using analytical solution for a good portion of the waveform. Finally, surrogate models (Field et al., 2014) use exclusively NR to compute waveforms on a limited parameter space, making them much more precise but with some setbacks, such as finite time intervals and no results in extremes of the parameter space due to lack of NR material. Surrogate models can be used over EOB or even hybrid models to improve the speed of computation.

When taking tidal effects into account, two types of corrections to BBH models are applied in order to capture the effects of tidal deformations on the morphology of the waveform. The first one is a phase shift occurring during the inspiral, on which most efforts to improve current models (such as NRTidal, see Dietrich et al. (2019)) are focused. The second one is a correction on the waveform's amplitude in order to model tidal disruption, which would cause the amplitude to suddenly decrease. In NSBH models, the phase shift in the inspiral is yet too hard to detect (it has only been detected in particularly strong BNS signals, see Abbott et al. (2017)). The point at which tidal disruption occurs is still not very well constrained. Currently, it is believed to only occur at mass ratios lower than 8 ($q < 8$), making both NSBH detections (q around 4) interesting cases. The lack of tidal disruption telltales in the amplitude of the signals may hint at equations of state describing more compact neutron stars, harder to disrupt, but it may very well be due to detection sensitivity and model precision being too poor. The insignificance of tidal effects detected so far with the current sensitivity is the reason why using uncorrected BBH models on non-disrupting NSBH signals is most sensible for the time being.

2.5   NSBH observations to date

Already before the first detection of gravitational waves, 19 binary neutron star systems had been identified in our Galaxy in the past four decades, and astrophysical models predicted the event rates of ground based gravitational wave detectors to be dominated by signals from binary black holes. Mixed neutron star-black hole binaries had however
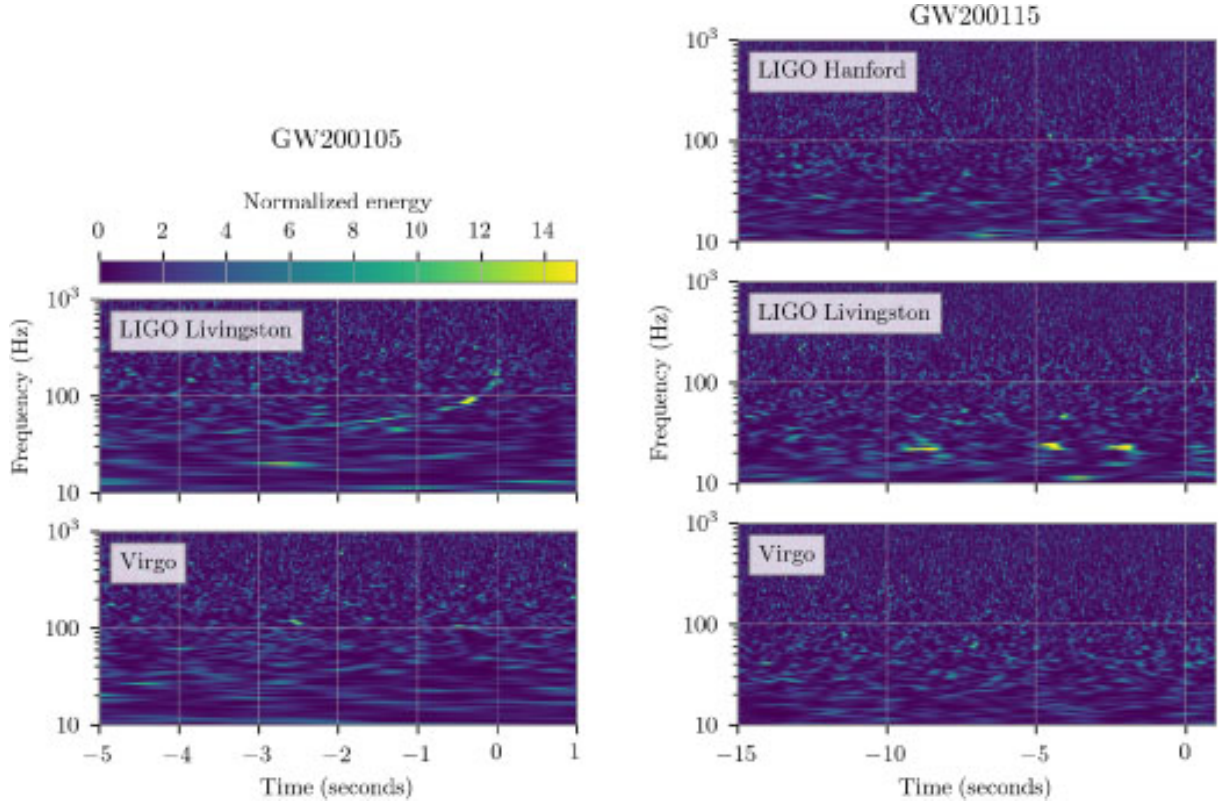
Figure 4: Data of the normalized energy carried by the gravitational radiation emitted by GW200105 (left column) and GW200115 (right column) represented in the time-frequency space. The spots that stand out in the GW200105 data from the LIGO Livingston detector below 25Hz correspond to light-scattering noise are shown after glitch subtraction. For GW200105, the LIGO Livingston data are shown after glitch subtraction. Image recovered from Abbott et al. (2021).

remained elusive in both EM and GW surveys before the third LIGO-Virgo observation run (O3), and the discovery of a pulsar in an NSBH binary remains a key objective for current and future radio observations. On the other hand, surveys in the Milky way show X-ray binaries with a BH component, which according to binary evolution models are one of the possible progenitors of NSBH binaries. The absence of NSBH candidates in LIGO's and Virgo's first two observing runs (O1 and O2) indicated an upper limit on the local merger rate density of NSBH systems of $\mathcal{R}_{NSBH} \leq 610 Gpc^{-3} yr^{-1}$ (all measurements are quoted at the 90% credible level).

Distinguishing between black holes and neutron stars in gravitational wave observations is difficult: EM counterparts can indicate the presence of a neutron star in a binary, but such counterparts are expected to be rare. Tidal deformation can influence the gravitational wave signal as discussed below, but is a sub-dominant effect and hard to detect. The main criterion thus is a mass larger than 3 $M_\odot$, the upper limit of neutron star masses, as discussed above.

During O3a, two events stood out as possible NSBH candidates, based on the observed masses of the components. First, GW190426_152155 (Abbott et al. 2021b) was identified as a marginal NSBH candidate with a high false-alarm rate (FAR; 1.4 yr^{-1}), it this could also plausibly be a noise artifact. The second event is GW190814 (Abbott et al. 2020c). Although the mass of GW190814 smaller component, $m_2 = 2.59^{+0.08}_{-0.09} M_\odot$, probably exceeds
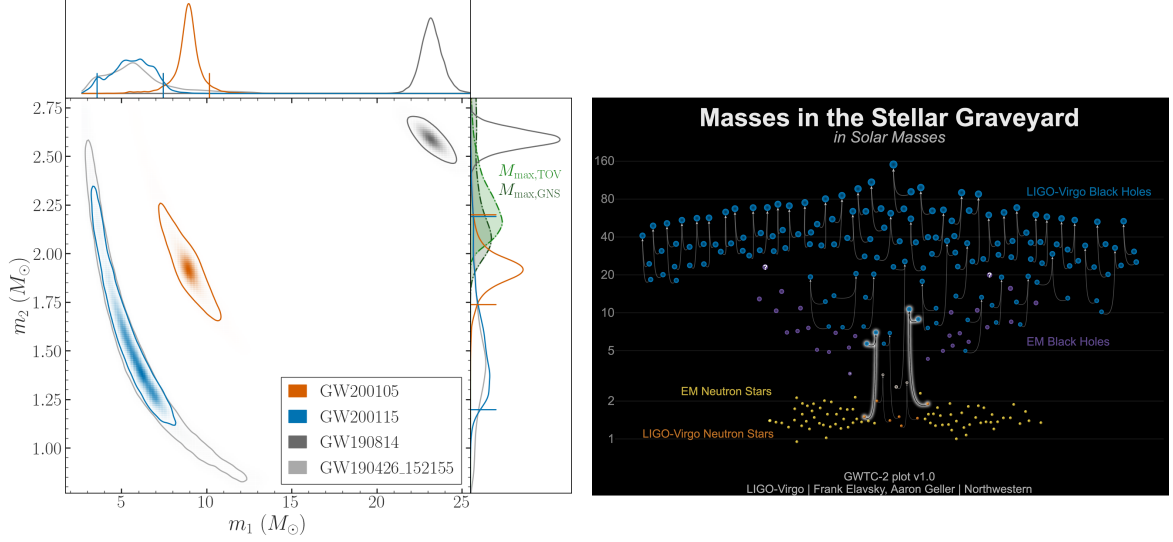
Figure 5: Left panel: Summary of the known component masses of the objects that produced GW200105 and GW200115, and also the two O3a NSBH candidates. The color-shading marks mass-combinations consistent with the data, with darker shading denoting better agreement, i.e. a higher probability for such mass-combinations. The top panel shows the information about the primary mass m_1 (black hole). The right panel summarizes the information about the secondary mass m_2, where green shadings represent the current astronomical knowledge about the maximal mass of neutron stars (one using the TOV equation explained in Subsection 2.2.2), showing that the secondary masses observed for all events (except possibly GW190814) are small enough to be neutron stars. Image recovered from Abbott et al. (2021). Right panel: The masses of black holes and neutron stars measured through EM observations (purple and yellow, respectively) and GW (blue and orange, respectively). The NSBH signals, GW200105 and GW200115, are highlighted as the merger of neutron stars with black holes. Image recovered from LIGO Science Summaries.

the maximal mass supported by slowly spinning NSs, it could be a NS spinning near its breakup frequency. Otherwise, it is the lightest BH ever detected. After the O3a run, of the 59 gravitational-wave signals that have had been detected, only two had properties consistent with NSBH binaries (Abbott et al., 2021).

In January of 2020, however, two further gravitational-wave signals were detected within the span of fifteen days, both of them with a high probability of having been caused by NSBH binaries. Assuming these events as representatives of their population, the local merger rate density of NSBH systems inferred is narrowed down to $\mathcal{R} \leq 45^{+75}_{-33} Mpc^{-3}yr^{-1}$. Inferring the local merger density rate assuming a broader distribution of component masses instead, yields $\mathcal{R} \leq 130^{+112}_{-69} Mpc^{-3}yr^{-1}$.

The first NSBH detection, GW200105_162426 (nicknamed GW200105), was detected on the fifth of January only by the LIGO Livingston and Virgo detectors, since the LIGO Hanford detector was not operative. But it was effectively a single-detector event in LIGO Livingston due to the small SNR in Virgo. The second one, GW200115_042309 (nicknamed GW200115), was a coincident detection of all three interferometers confidently targeting it as an astrophysical GW event. Figure 4 shows the time-frequency representation of the two event. The top left panel shows the time-frequency data of

GW200105, were a track of excess power with increasing frequency stands out. No similar tracks are visible in the other panels as the SNR is lower in each of the detectors and the signal is longer for GW200115. We can also see light-scattering noise in LIGO Livingston at around 20 Hz.

To infer the physical properties of the sources of GW200105 and GW200115, a parameter estimation was conducted via a coherent Bayesian analysis of data from all detectorsr (except LIGO Hanford for GW200105, since it was inoperative). Due to the different duration of the signals, up to 64 seconds were analyzed of the GW200115 signal, and only 32 seconds of the higher mass signal. A low-frequency cut-off was set at $f_{low} = 20Hz$ for all likelihood evaluations except for the LIGO Livingston detection of GW200115, which was set at 25 Hz to avoid the light-scattering noise. Parallel Bilby (PBILBY) and DINESTY nested sampling software were the main tools used to sample posterior distribution of the sources parameters, as well as RIFT for the most computational expensive analyses and LALINFERENCE for verification. The waveform models used as base for the main analyses of both signals were BBH models with spin induced orbital precession and higher order multipole GW moments, although they do not include tidal effects. Specifically, one of each BBH waveform model families were used: IMRPhenomXPHM and SEOBNRv4PHM. Of course, the impact of neglecting tidal effects should be quantified; and for that, two NSHB models with tidal effects were used to analyse the waveform assuming all spins were aligned with the orbital angular momentum and their values restricted to the region of applicability of NSBH models, i.e. $\chi_1 = 0.5$ and $\chi_2 = 0.05$ for the PhenomNSBH model and $\chi_1 = 0.9$ and $\chi_1 = 0.05$ for the EOBNR model. After that, analyses performed with aligned-spin BBH waveform models found good agreement with those performed with NSBH models, further validating the use of BBH waveform models to analyze the two NSBH signals. Specifically, two models using only dominant quadruple moment (IMRPhenomXAS and SEOBNRv4) and two others with higher order moments (IMRPhenomXHM and SEOBNRv4HM).

There is no direct evidence indicating that the secondary masses are NSs, since neither tidal disruption nor other tidal effects were measured and no EM counterparts were found for either detection. Therefore, both detections are compatible with BBH merger signals. However, given the properties and distances of the two events, the absence of tidal measurements and EM counterparts is to be expected. Nevertheless, parameter estimation for the component masses sets the primary objects within the BH mass range and yields values for the secondary objects that suggest they indeed are NSs. Concretely, the primaries have masses of $8.9^{+1.2}_{-1.5}M_\odot$ and $5.7^{+1.8}_{-2.1}M_\odot$, for GW200105 and GW200115 respectively, which is well beyond the NS maximal mass and within the range of BH observed through both electromagnetic and gravitational radiation. Therefore we can confidently assume them to be BH. The secondaries have masses of $1.9^{+0.3}_{-0.2}M_\odot$ and $1.5^{+0.7}_{-0.3}M_\odot$ which, when compared to the maximum allowed NS mass, fall within the known range of NS masses with probabilities of 89%-96% and 87%-98%, respectively. See Figure 5 (left panel) for the probability distributions of these masses, as well as those of both O3a candidates mentioned before.

Owing to the nature of the detections, location of the sources is not very well constrained. Both signals were found to be born at great luminosity distances, $D_L = 280^{+110}_{-110}$ and $D_L = 300^{+150}_{-100}$ for GW200105 and GW200115, respectively. Sky location accuracy differs significantly between detections, however, owing to one being an effective single-detector event and the other a joined detection. The source of GW200105, was localized to sky area of 7200 deg^2, whereas GW200115's, was localized within 600 deg^2, an order
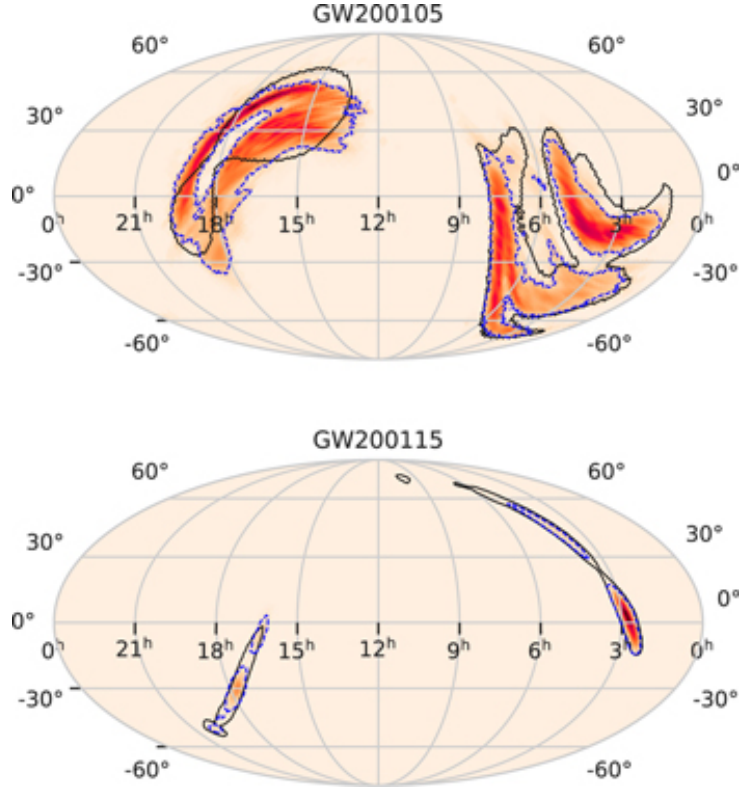
Figure 6: Sky localization for GW200105 (top) and GW200115 (bottom) in terms of right ascension and declination. The shaded patch is the sky map obtained from the preferred high-spin analysis, with the 90% credible regions bounded by the thin dotted contours. The thick solid contours show the 90% credible regions from the low-latency sky localization algorithm BAYESTAR. Image recovered from Abbott et al. (2021).

of magnitude smaller thanks to the presence of the data of LIGO Hanford (see Figure 6).

The evolutionary history of binary systems can be probed with the spin information encoded in the gravitational waves they emit. Therefore, its study is of significance when trying to discern the binary's formation and its components origin. A useful magnitude to describe the spin of binary components is dimensionless spin, $\boldsymbol{\chi}_i$, whose magnitude $(\chi_i \equiv |\boldsymbol{\chi}_i|)$ is bounded by 1 for black holes (the rotation speed of the horizon is limited by the speed of light) and which is related to angular momentum $\mathbf{S}_i$ by $\boldsymbol{\chi}_i = c\mathbf{S}_i/(Gm_i^2)$. From this, we can define the effective inspiral spin parameter, which is one of the best-constrained parameters and encodes information about the binaries' spin components parallel to the orbital angular momentum, $\chi_{eff} = (\frac{m_1}{M}\chi_1 + \frac{m_2}{M}\chi_2) \cdot \hat{L}$, where $\hat{L}$ is the unit vector along the orbital angular momentum.

The primary spins inferred for both signals are consistent with EM observations and predictions of BH spins given by models of stellar and dynamical evolution of NSBH progenitors. Context of predictions of BH spins given by models of stellar and dynamical evolution and EM observations of NSBH progenitors finds agreement with primary spins inferred for both signals being representative of BH population. Secondary spins, however, are poorly constrained due to unequal mass between the components in both signals; although pulsar timing observations of binaries that merge within a Hubble time imply a highest dimensionless spin of ~ 0.04. Spin magnitudes and orientation of black holes in binaries are expected to span a varied range depending on the formation of the binary. Bayesian inference yields posterior values of $\chi_{eff} = -0.01^{+0.11}_{-0.15}$ for GW200105,

which is strongly peaked around zero, and $\chi_{eff} = -0.19^{+0.23}_{-0.35}$ for GW200115, which supports a negative projection over the orbital momentum ($\chi_{z,1} = -0.19^{+0.24}_{-0.50}$) with an 88% probability. More negative values of $\chi_{z,1}$ than that are correlated with particularly small primary masses reaching into the lower mass gap ($3M_\odot < m_1 < 5M_\odot$). The probability found for that scenario are 30% or 27%, each corresponding to the high-spin and low-spin parameter estimation priors used to infer all given values, respectively.

Binary systems can also show the phenomenon of spin precession when at least one of the components has a spin component in the orbital plane of the binary, however it turns out that at the SNRs observed so far, precession is very hard to measure. The spins are typically parameterized using the effective precession spin parameter, χ_p, which is essentially the magnitude of the spin in the orbital plane of the larger component. For GW200105 and GW200115, $\chi_p = 0.09^{+0.14}_{-0.07}$ and $\chi_p = 0.21^{0.30}_{-0.17}$ were inferred respectively, although attempts to assess the significance of a measurement of precession yielded inconclusive evidence. This was expected, however, due to the given SNRs and inferred inclination angles of the orbits.

Low values of primary mass are strongly correlated with a negative projection of its spin over the orbital angular momentum ($\chi_{1,z} < 0$), and therefore consistent with dynamical capture as the binary formation channel, since it should produce random orientation of the components' spins within the orbit. Rates of such formation channel are unknown, however, since predictions carry huge uncertainties. On the other hand, binaries formed in isolation are expected to show small misalignments, but spin may misalign through other processes, such as the kick of a supernova explosion and subsequent evolution via mass transfer. Also, progenitor binaries born in young clusters can be perturbed by close dynamical encounters before being thrown out of them. Thus, primary spin misalignment does not suffice to discard any of the possible NSBH formation channels.

3   Analysis of NSBH waveforms

The aim of this section is to conduct a rough estimate of the validity of the analysis of NSBH signals and the significance of systematic errors using different waveform models, some mentioned in Subsection 2.4. To achieve that, I have computed the mismatch $\mathcal{M} = 1 - m$ (m being the match, defined in (2.43)), between pairs of templates from these models (obtained from the open source LIGO Algorithm Library (LAL) (LIGO Scientific Collaboration, 2018)) instead of matching a template to the detector's output. These calculations have been conducted in the frequency domain for the dominant spherical harmonic mode ($l = 2, m = 2$) and within a discrete spin-spin parameter space in the form of gridded mismatches, using functions from PyCBC (a software package used to explore astrophysical sources of gravitational waves (Nitz et al., 2021)), in a python script.

In order to evaluate the significance of the mismatch, one can almost qualitatively associate it with the SNR needed to be able to distinguish the discrepancies of the results the paired models yield:

$$\mathcal{M} < \frac{D}{2\rho^2} \,, \tag{3.1}$$

where $\mathcal{M}$ is the value of the mismatch, D is the number of model parameters (7 for a binary system using the geometrized coordinates) and ρ is the minimum value of SNR below which the mismatch $\mathcal{M}$ is imperceptible (Boyle et al., 2019). Thus, we can convert the gridded matches plotting the minimum value of ρ corresponding to every value of $\mathcal{M}$
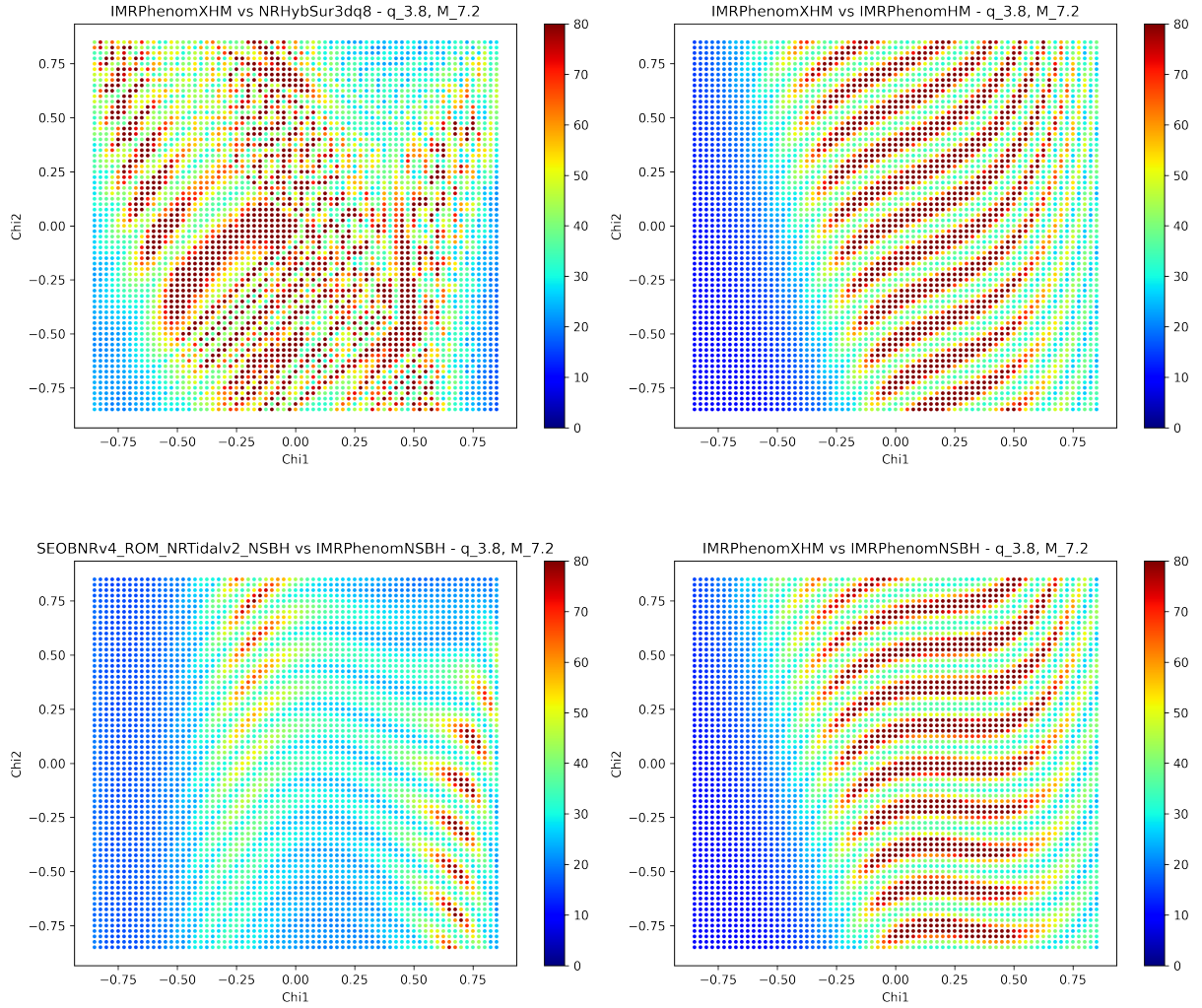
Figure 7: Mismatches of the labeled models translated to SNR value needed for the dissagreement between them to be significant. All computed for a spin-aligned orbit of mass ratio $q = 3.8$ and total mass $M = 7.2 M_{\odot}$, which correspond to the expected posterior values of GW200115 and are representative of low primary mass NSBH systems. The axis variables "Chi1" and "Chi2" correspond to the primary and secondary spins, respectively.

on each point of the parameter space,

$$\rho_{min} = \sqrt{\frac{D}{2\mathcal{M}}}. \tag{3.2}$$

Taking this angle into the analysis of mismatches, we can study whether the possible systematic errors (about which we know very little) committed in the process are significant compared to the statistical errors of Bayesian inference based on matched filtering in terms of the SNR values of the detections. Within the context of current sensitivity, we find most detections have SNR values between 10 and 15, with the loudest signals at around 30. This means that for points in the parameter space at which the mismatch of the different models yield SNR thresholds below 30, we cannot neglect the possible systematic errors and should consider those models unreliable. Moreover, upgrades planned for the O4 run are expected to at least double the sensitivity, thus hoisting the SNR

24

threshold up to around 70 and rendering most of the current models unreliable in most of the parameter space, as we will see in the following discussion of the plots. Matches between five different models have been performed, of which only the four that yield the most significant results are shown in Figure 7.

In all of them we can see, in more or less measure, that discrepancies increase at high absolute values of the primary spin (although most notably in the negative spectrum), indicating its significance over the value of the secondary spin in these calculations, as would be expected for binaries with very unequal masses. However, the effects of secondary spin are also noticeable, making the region of high negative spins the most troublesome.

The top left panel (match between IMPRPhenomXHM and a surrogate and hybrid model) shows low levels of mismatch consistent with the high agreement of modern models. On one hand, PhenomX is one of the latest families of phenomenological models, and Hybrid Surrogate models, as explained in section 2.4, can yield results with high precision albeit for concrete regions of the parameter space. Therefore, high levels of SNR would be needed to discern this mismatch and raise the issue of possible systematic errors. The only troublesome regions would be high positive primary spin, high negative primary spin with negative secondary spin, and positive primary spin with high positive negative spin. Notice that with the expected sensitivity of O4 run this will no longer be true, since SNR values around 50 are anticipated to be commonplace.

The models of the top right panel (match between old and new higher order models from the Phenom family) differ in a significant portion of the parameter space, mainly medium-high negative primary spin. This showcases the improvement accomplished with Phenom family upgrades in that most challenging region.

The bottom left panel (match between Effective-One-Body and Phenomenlogical NSBH models) presents a very low SNR threshold for mismatch detection in most of the parameter space (notice the strange behaviour in the high mismatch area at low primary spin), which proves they are not yet reliable for medium-high SNR detections even with the current sensitivity.

The bottom right panel (match between IMRPhenomXHM and IMRPhenomNSBH) exhibits a very similar plot to the top right's, owing to the fact that NSBH models are mostly amplitude corrections to older models, as PhenomNSBH is to PhenomHM. These corrections are yet to be done to newer and more improved models, which could possibly yield more accurate models describing NSBH systems.

An extended analysis of the mismatch variations when modifying the mass ratio and total mass of the binary system is not possible, since these two parameters are very limited in the parameter space to allow the use of all the models implemented; namely the surrogate model which, as explained in section 2.4, does not work for high values of both q and M, and the NSBH models, which restrain secondary masses below $3M_\odot$. Since the focus of this project is NSBH binaries, we can restrain our analysis to this region of the parameter space. Thus, Figure 8 shows a comparison between high and low mass ratios for a fixed total mass within the allowed range. There, we can clearly see that for a higher mass ratio, the primary spin becomes more significant, exhibiting high levels of mismatch at high absolute values; whereas for lower mass ratio, good results are obtained in a larger portion of the parameter space, and the effect of negative secondary spin becomes more noticeable.

Nevertheless, to see the setbacks of being confined in this region of the parameter space, we can use the BBH models to compare our mismatch to one corresponding to higher total mass binary systems. Thus, four plots are shown in Figure 9 for higher-mass
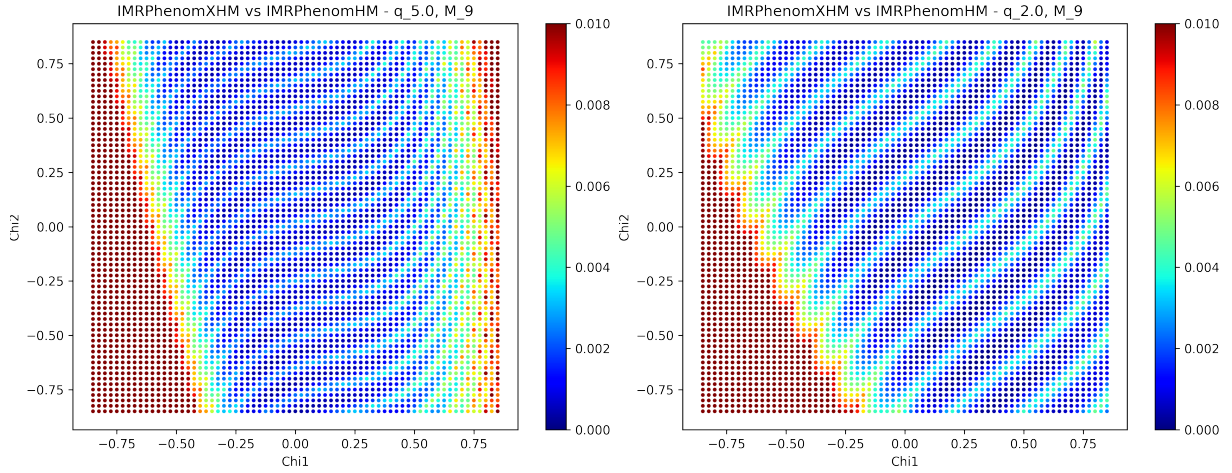
Figure 8: Comparison of the mismatch $\mathcal{M}$ between IMRPhenomHM and IMRPhenomXHM for mass ratios q=2 and q=5 at fixed total mass M=9. The axis variables "Chi1" and "Chi2" correspond to the primary and secondary spins, respectively.

binaries. As mentioned in other sections, high-mass binaries emit at lower frequencies. This entails two consequences responsible of the dramatic change in the shape of the gridded mismatch. The first one, is the shift between the sensitivity frequency distribution and the signal, changing which phases of the coalescence we detect at high or low SNR, and thus transferring the disagreement between models to other regions of the parameter space: until now we have seen the most disagreement at high negative spins, where now we observe very low levels of mismatch. The second one is related to the amount of information we obtain from the detection. As seen in Eq. (2.17), for higher chirp mass we are able to detect less cycles before the merger. From left to right and top to bottom, the number of cycles we detect given the chirp masses of each binary (see caption) are 274, 171, 37 and 23, respectively. This lack of information compared to lower chirp mass binaries (a few thousand cycles detected) negatively impacts our ability to distinguish between different waveforms, so the differing results of each model become less noticeable. Notice how the low mismatch region in the plots of Figure 9 increases with the chirp mass. On the other hand, however, this means that for low chirp mass binaries we are not learning all the information we could, because our models are unable to discern between different waveforms at the level at which would be possible given the amount of information we are getting; hence the higher mismatches.
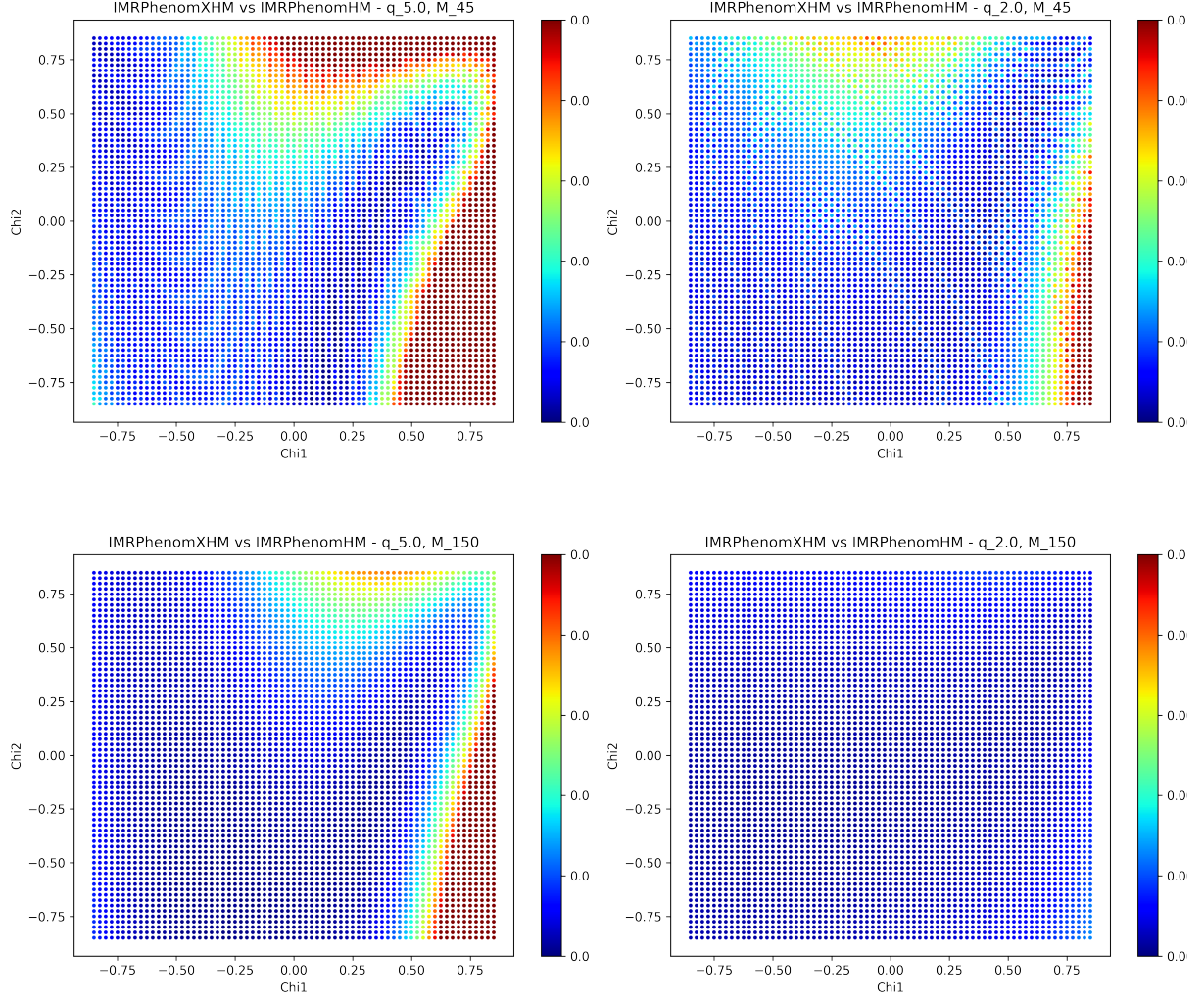
Figure 9: Mismatches between PhenomHM and PhenomXHM. Mass ratio and total mass correspond to component masses of: $m_1 = 37.5 M_\odot$ and $m_2 = 7.5 M_\odot$, with chirp mass $M_c = 14 M_\odot$ (top left panel); $m_1 = 3o M_\odot$ and $m_2 = 15 M_\odot$, with chirp mass $M_c = 18 M_\odot$ (top right panel); $m_1 = 125 M_\odot$ and $m_2 = 25 M_\odot$, with chirp mass $M_c = 46 M_\odot$ (bottom left panel); and $m_1 = 100 M_\odot$ and $m_2 = 50 M_\odot$, with chirp mass $M_c = 61 M_\odot$ (bottom right panel). The axis variables "Chi1" and "Chi2" correspond to the primary and secondary spins, respectively.

4   Conclusions

This work consists of an overview on the basics of gravitational wave theory and the physics governing compact bodies, in order to better understand the current status on detection and waveform modeling of signals from binary systems, specifically Neutron Star-Black Hole binaries, as well as their reliability and systematic error significance. For that, mismatches between different models have been conducted, arriving to the conclusion that, for the design sensitivity expected to be achieved in O4, the waveform models will require improvement in order to accurately match the new flood of information we will receive; most notably NSBH models, which will be needed to characterize the equation of state of neutron stars a the tidal corrections to the gravitational emission, and were already behind in the O3 runs.

First, after obtaining the gravitational-wave solution in linearized theory, the first order newtonian approximation, quadrupole approximation, was applied in order to obtain analytic results, allowing to represent some typical numbers for specific cases. Then, the line element for both static and rotating black holes was explained, as well as for space-times with matter, until getting to the Tolkov-Oppenheimer-Volkov equation, from which we extracted a simplified equation of state and an expression for maximal mass that would help better understand the characteristics of Neutron Star-Black Hole binary systems and the gravitational-wave radiation they emit, such as the effects of tidal interaction and tidal disruption. In addition, a summarize of the physics governing compact object formation and composition was done to better explain said effects. After that, an overview of the detection process and data analysis was given describing the signal-to-noise ratio and the match-filtering technique later used in the plots, as well as of the history and current state of BBH and NSBH waveform models. In order to contextualize all the above in a real framework, a run-through of the currently only two NSBH detections characteristics is given, which have provided brand new information on the elusive NSBH systems. Finally, an analysis of the reliability of different models was conducted in terms of SNR, in order to ascertain the regions of a spin-spin parameter space for distributions similar to the NSBH detections at which the systematic errors may become significant compared to the statistical errors of the data analysis. Thus concluding that information on the NSBH coalescences is being lost due to lack of precision of the current NSBH models, and also that when the O4 planned sensitivity is achieved, the systematic errors of which we know very little may become an issue.

To summarize, an increase of sensitivity would allow detections of sources further away and at longer times before coalescence, but it would also allow to better observe and understand waveform modifications due to tidal effects in the inspiral, getting us closer to figuring out specific equations of state of compact objects like neutron stars or white dwarfs. However, this upgrades on the sensitivity will also bring the models discrepancies into view, rendering them unreliable. Therefore, NSBH models will need a huge improvement in order to accurately match the signals we will detect. Otherwise, we will not be able to infer faithful data to correctly characterize the equations of state or model tidal disruption.

References

Abbott, B. P., and Coauthors, 2017: GW170817: Observation of gravitational waves from a binary neutron star inspiral. *Phys. Rev. Lett.*, **119**, 161 101.

Abbott, R., and Coauthors, 2021: Observation of gravitational waves from two neutron star–black hole coalescences. *The Astrophysical Journal Letters*, **915 (1)**, L5.

Ajith, P., and Coauthors, 2011: Inspiral-merger-ringdown waveforms for black-hole binaries with nonprecessing spins. *Phys. Rev. Lett.*, **106**, 241 101.

Amaro-Seoane, P., and Coauthors, 2013: eLISA: Astrophysics and cosmology in the millihertz regime. *GW Notes*, **6**, 4–110, arXiv:1201.3621.

Amaro-Seoane, P., and Coauthors, 2017: Laser interferometer space antenna. arXiv:1702.00786.

Boyle, M., and Coauthors, 2019: The SXS collaboration catalog of binary black hole simulations. *Classical and Quantum Gravity*, **36 (19)**, 195 006.

Chandrasekhar, S., 1931: The Maximum Mass of Ideal White Dwarfs. *The Astrophysical Journal*, **74**, 81.

Dietrich, T., A. Samajdar, S. Khan, N. K. Johnson-McDaniel, R. Dudi, and W. Tichy, 2019: Improving the nrtidal model for binary neutron star systems. *Phys. Rev. D*, **100**, 044 003.

Field, S. E., C. R. Galley, J. S. Hesthaven, J. Kaye, and M. Tiglio, 2014: Fast prediction and evaluation of gravitational waveforms using surrogate models. *Phys. Rev. X*, **4**, 031 006.

Goldberg, J. N., A. J. Macfarlane, E. T. Newman, F. Rohrlich, and E. C. G. Sudarshan, 1967: Spin-s spherical harmonics and ð. *Journal of Mathematical Physics*, **8 (11)**, 2155–2161.

Harry, I. W., and S. Fairhurst, 2011: Targeted coherent search for gravitational waves from compact binary coalescences. *Phys. Rev. D*, **83**, 084 002.

Hulse, R. A., and J. H. Taylor, 1975: Discovery of a pulsar in a binary system. *The Astrophysical Journal*, **195**, L51–L53.

Israel, W., 1967: Event Horizons in Static Vacuum Space-Times. *Physical Review*, **164 (5)**, 1776–1779.

Israel, W., 1968: Event horizons in static electrovac space-times. *Communications in Mathematical Physics*, **8 (3)**, 245–260.

Kerr, R. P., 1963: Gravitational Field of a Spinning Mass as an Example of Algebraically Special Metrics. *Phys. Rev. Lett.*, **11 (5)**, 237–238.

LIGO Scientific Collaboration, 2018: LIGO Algorithm Library - LALSuite. free software (GPL).

MacDonald, I., S. Nissanke, and H. P. Pfeiffer, 2011: Suitability of post-newtonian/numerical-relativity hybrid waveforms for gravitational wave detectors. *Classical and Quantum Gravity*, **28 (13)**, 134 002.

Maggiore, M., 2008: *Gravitational waves: Volume 1: Theory and experiments*, Vol. 1. Oxford university press.

Martynov, D. V., and Coauthors, 2016: Sensitivity of the advanced ligo detectors at the beginning of gravitational wave astronomy. *Phys. Rev. D*, **93**, 112 004.

Newman, E. T., and A. I. Janis, 1965: Note on the Kerr Spinning-Particle Metric. *Journal of Mathematical Physics*, **6 (6)**, 915–917.

Nitz, A., and Coauthors, 2021: gwastro/pycbc:. Zenodo.

Nordström, G., 1918: On the Energy of the Gravitation field in Einstein's Theory. *Koninklijke Nederlandse Akademie van Wetenschappen Proceedings Series B Physical Sciences*, **20**, 1238–1245.

Peters, P. C., 1964: Gravitational radiation and the motion of two point masses. *Phys. Rev.*, **136**, B1224–B1232.

Pratten, G., S. Husa, C. García-Quirós, M. Colleoni, A. Ramos-Buades, H. Estellés, and R. Jaume, 2020: Setting the cornerstone for a family of models for gravitational waves from compact binaries: The dominant harmonic for nonprecessing quasicircular black holes. *Phys. Rev. D*, **102**, 064 001.

Reissner, H., 1916: Über die Eigengravitation des elektrischen Feldes nach der Einsteinschen Theorie. *Annalen der Physik*, **355 (9)**, 106–120.

Rettegno, P., F. Martinetti, A. Nagar, D. Bini, G. Riemenschneider, and T. Damour, 2020: Comparing effective-one-body hamiltonians for spin-aligned coalescing binaries. *Phys. Rev. D*, **101**, 104 027.

Schwarzschild, K., 1916: On the Gravitational Field of a Mass Point According to Einstein's Theory. *Abh. Konigl. Preuss. Akad. Wissenschaften Jahre 1906,92, Berlin,1907*, **1916**, 189–196.

Tsang, D., J. S. Read, T. Hinderer, A. L. Piro, and R. Bondarescu, 2012: Resonant shattering of neutron star crusts. *Phys. Rev. Lett.*, **108**, 011 102.

Usman, S. A., and Coauthors, 2016: The PyCBC search for gravitational waves from compact binary coalescence. *Classical and Quantum Gravity*, **33 (21)**, 215 004.

Veitch, J., and Coauthors, 2015: Parameter estimation for compact binaries with ground-based gravitational-wave observations using the lalinference software library. *Phys. Rev. D*, **91**, 042 003.

Wald, R. M., 1984: *General Relativity*. Chicago Univ. Press, Chicago, USA.

Wikipedia, 2021: Type Ia supernova — Wikipedia, the free encyclopedia. http://en.wikipedia.org/w/index.php?title=Type%20Ia%20supernova&oldid=1040440277.